The translational landscape of SARS-CoV-2 and infected cells

Maritza Puray-Chavez[1,*], Kasyap Tenneti[1,*], Hung R. Vuong[1, *], Nakyung Lee[1,*], Yating Liu[2], Amjad Horani[3], Tao Huang[4], Sean P. Gunsten[4], James B. Case[5], Wei Yang[2], Michael S. Diamond[1,5,6], Steven L. Brody[4], Joseph Dougherty[2,7], Sebla B. Kutluay[1]

[1] Department of Molecular Microbiology, Washington University School of Medicine, Saint Louis, MO 63110, USA

[2] Department of Genetics, Washington University School of Medicine, Saint Louis, MO 63110, USA

[3] Department of Pediatrics, Allergy, Immunology and Pulmonary Medicine, Washington University School of Medicine, Saint Louis, MO 63110, USA

[4] Department of Medicine, Pulmonary and Critical Care Medicine, Washington University School of Medicine, Saint Louis, MO 63110, USA

[5] Department of Medicine, Infectious Disease Division, Washington University School of Medicine, Saint Louis, MO 63110, USA

[6] Department of Pathology & Immunology, Washington University School of Medicine, Saint Louis, MO 63110, USA

[7] Department of Psychiatry, Washington University School of Medicine, Saint Louis, MO 63110, USA

Correspondence: Kutluay@wustl.edu

Highlights

- Ribo-seq reveals key translationally regulated events in SARS-CoV-2 replication
- SARS-CoV-2 frameshifting is substantially more efficient than HIV-1
- SARS-CoV-2 infection results in transcriptional upregulation of inflammatory and interferon-stimulated genes
- SARS-CoV-2 disarms host responses at the level of mRNA translation

Summary

SARS-CoV-2, a betacoronavirus with a positive-sense RNA genome, has caused the ongoing COVID-19 pandemic. Although a large number of transcriptional profiling studies have been conducted in SARS-CoV-2 infected cells, little is known regarding the translational landscape of host and viral proteins. Here, using ribosome profiling in SARS-CoV-2-infected cells, we identify structural elements that regulate viral gene expression, alternative translation initiation events, as well as host responses regulated by mRNA translation. We found that the ribosome density was low within the SARS-CoV-2 frameshifting element but high immediately downstream, which suggests the utilization of a highly efficient ribosomal frameshifting strategy. In SARS-CoV-2-infected cells, although many chemokine, cytokine and interferon stimulated genes were upregulated at the mRNA level, they were not translated efficiently, suggesting a translational block that disarms host innate host responses. Together, these data reveal the key role of mRNA translation in SARS-CoV-2 replication and highlight unique mechanisms for therapeutic development.

KEYWORDS: SARS-CoV-2, ribosome profiling, ribo-seq, mRNA translation, virus replication, ribosomal frameshifting, virus-host interaction, immune response, translational repression

INTRODUCTION

The Coronavirus (CoV) group encompasses of a number of single-stranded, positive-sense RNA viruses with unusually large genomes (27-32 kb), which infect a wide range of animal species, including humans (Masters, 2006, Weiss and Navas-Martin, 2005). Previously, outbreaks of two members of this group, severe acute respiratory syndrome (SARS-CoV) and Middle East respiratory syndrome (MERS-CoV), have caused lethal respiratory illnesses in 2002 and 2012, respectively (de Wit et al., 2016). Presently, SARS-CoV-2, the causative agent of the ongoing Coronavirus Disease-2019 (COVID-19) pandemic, has infected millions of people worldwide and has devastated the global economy. Currently, there are limited options for antiviral or immunomodulatory treatment against SARS-CoV-2, with only few therapies being currently recommended for more severe COVID-19 cases. A basic understanding of the replicative mechanisms of SARS-CoV-2 and associated host responses potentially can foster the development of virus-specific therapies.

The first two-thirds of the 5' end of the SARS-CoV-2 genome is composed of two overlapping open reading frames (ORFs), ORF1a and ORF1b, which encode for two polyproteins, pp1a and pp1ab (Nakagawa et al., 2016). Pp1a is produced when translation of the genomic RNA terminates at the stop codon of ORF1a. Pp1ab is generated via a programmed -1 ribosomal frameshift (PRF) that occurs at the overlap between ORF1a and ORF1b, permitting the elongating ribosomes to bypass the termination signal in ORF1a (Plant and Dinman, 2008). Following synthesis, pp1a and pp1ab are cleaved by viral proteases to generate 15-16 mature nonstructural proteins (nsp) (Nakagawa et al., 2016). Many proteins encoded in ORF1b, are part the replication complex, thus making the -1 PRF to generate pp1ab a critical translational event for SARS-CoV-2 replication. Frameshifting in coronaviruses is regulated by a highly conserved heptanucleotide slippery sequence (UUUAAAC) and an RNA pseudoknot structure a few nucleotides downstream (Plant and Dinman, 2008). The current models of PRF suggest that ribosomes stall upon encountering the pseudoknot (Plant et al., 2003, Korniy et al., 2019). This event presumably enhances the efficiency of ribosomal frameshifting by forcing the ribosomes to pause on the slippery sequence, which in turn promote the -1 slippage. Once the pseudoknot unwinds and resolves, the ribosome goes on to translate the alternate ORF.

Another well-known frameshifting mechanisms in human viruses is employed by retroviruses through a stem-loop structure that regulates the expression of Gag/Gag-Pol transcripts (Jacks et al., 1988, Wilson et al., 1988). Frameshifting here is thought essential for maintenance of the ratio of Gag and Gag-Pol polyproteins as well as viral infectivity (Shehu-Xhilaga et al., 2001, Garcia-Miranda et al., 2016). While frameshifting is thought to be highly inefficient in HIV-1, with only 5-10% of ribosomes continuing into the Pol ORF (Baril et al., 2003, Dulude et al., 2006, Jacks et al., 1988), CoV frameshifting is thought to occur at a much higher efficiency (Irigoyen et al., 2016). However, to date, the behavior of ribosomes within the frameshifting element for neither SARS-CoV-2 nor HIV-1 in infected cells has been empirically assessed.

In addition to hijacking the host translational machinery, SARS-CoV-2 can modulate host mRNA translation so as to suppress the immune system to ensure efficient propagation. Indeed, several viral proteins reportedly impair host gene expression post-transcriptionally (Lokugamage et al., 2012, Xiao et al., 2008, Kopecky-Bromberg et al., 2006, Huang et al., 2011, Zhou et al., 2008, Kamitani et al., 2009, Narayanan et al., 2008, Nakagawa et al., 2016). SARS-CoV nonstructural protein nsp1 induces endonucleolytic cleavage in the 5'-UTR of cellular mRNAs, accelerating their turnover, but not in viral mRNAs (Kopecky-

Bromberg et al., 2006). Furthermore, nsp1 tightly binds to the 40S ribosomal subunit and blocks translation initiation (Kamitani et al., 2009). This dual capacity to cleave host mRNAs and directly inhibit their translation may allow SARS-CoV-2 to overcome the type I IFN response in infected cells, as has been demonstrated for SARS-CoV (Narayanan et al., 2008). On the other hand, the bulk of published research on SARS-CoV- and SARS-CoV-2-host interactions has relied on transcriptional profiling to study the immune response to infection (Blanco-Melo et al., 2020, Butler et al., 2020, Menachery et al., 2014, Mitchell et al., 2013, Wilk et al., 2020, Zhou et al., 2020). Such approaches may not fully capture the host immune response to infection, in the face of viral mechanisms that block host mRNA translation.

Here, we have conducted in-depth ribosome profiling studies to gain insight into the role of translational regulation in SARS-CoV-2 replication and the resulting host responses. We found that ribosome occupancy on viral mRNAs was temporally regulated and partly dependent on RNA abundance. In addition, ribosomes engaged with novel translation initiation sites (TIS) and other potential regulatory elements on SARS-CoV-2 RNAs. Viral mRNAs encoding E, S and ORF1ab were more efficiently translated than other viral mRNAs, but the overall translation efficiency of viral mRNAs was not substantially different than cellular mRNAs. In addition, we found that ribosomes were depleted rather than enriched on the SARS-CoV-2 frameshifting site and SARS-CoV-2 frameshifting was more efficient than HIV-1. Remarkably, while numerous inflammatory chemokines, cytokines and ISGs were upregulated transcriptionally in SARS-CoV-2-infected cells, we found that many were not efficiently translated. Overall, our study defines the translational landscape of SARS-CoV-2-infected cells, revealing novel events that may promote viral replication and disarm host immune responses at the level of mRNA translation.

RESULTS

Ribosome profiling reveals key features of SARS-CoV-2 translational program

To study the relationship between transcriptionally and translationally regulated events at early and late phases of SARS-CoV-2 infection, Vero E6 cells infected at low and high multiplicity of infection (MOIs, 0.1 and 2 plaque forming units [PFU]/cell, respectively)) were monitored by RNA-seq and ribo-seq during the course of infection (**Fig. 1A**). Viral antigen staining of infected cells revealed that the majority of the cells were infected by 24 hpi for low MOI and by 12 hpi for high MOI infections (**Fig. S1A, S1B**). High quality duplicate sequencing libraries with favorable mapping statistics were generated (**Tables S1-S4)**. The quality of each ribo-seq library was assessed as follows. First, the length of distribution of ribo-seq reads that mapped to cellular and viral transcriptomes were within the expected range of ribosome protected fragments (**Fig. S2A, S2B, S3A, S3B**) (Ingolia et al., 2012, Ingolia et al., 2009). We noted that in one experiment read lengths trended to be longer likely due to lesser extent of nuclease digestion (**Fig. S3A, B**). Second, the majority of ribo-seq reads mapped to coding sequences and 5' UTRs, with clear reduction in the fraction of reads mapping to 3'UTRs when compared to RNA-seq experiments done in parallel (**Fig. S2C, Fig. S4**). Third, mapped ribosome footprints within the CDSs were enriched in fragments that align to the translated frame (**Fig. S2D, Fig. S5**).

For low MOI infections, ~50% of the uniquely mapping RNA-seq reads were derived from SARS-CoV-2 mRNAs by 24 hours post infection (hpi) (**Fig. 1B**). By 48 hpi >80% of the uniquely mapping reads were viral (**Fig. 1B**) demonstrating that viral mRNAs quickly dominate the total cellular mRNA pool. The percentage of SARS-CoV-2-derived mRNAs did not increase further at 72 hpi (**Fig. 1B**), partly due to virus-induced cytotoxicity. Comparatively, a smaller percentage of ribosome-associated mRNAs were derived from

SARS-CoV-2, approximating 20 to 40% at early and late time points in infection, respectively (**Fig. 1C**). Despite their relative abundance in the cytosol, viral RNAs were not specifically enriched in ribosome-bound pool. As we observed significant levels of cytotoxicity at 72 hpi, we focused our analyses on the earlier 24 and 48 hpi time points.

Plotting of RNA-seq reads on the viral genome demonstrated that N-derived sgRNAs were highly abundant throughout infection (**Fig. 1D-E, and S5**), a finding consistent with previous RNA-seq studies (Kim et al., 2020, Huang et al., 2020). Expectedly, the majority of these reads were derived from positive sense viral mRNAs, albeit substantially lower copies of anti-sense transcripts were also detectable (**Fig. S6**). Furthermore, ribosomes were enriched on N mRNAs, with a high peak surrounding the translation start site, at 24 hpi (**Fig. 1D**). As expected from the low abundance of ORF10 encoding sgRNAs, we noted that ribosome occupancy fell abruptly after the N stop codon, although footprints were still detectable within the ORF10 coding sequence with an average read count of 136 per nucleotide, A second high ribosome occupancy site was observed within the M ORF at 24 hpi, again with a distinct peak around the translation start site (**Fig. 1D**). ORFs downstream from S also were bound by ribosomes, albeit at lower levels (**Fig. 1D**). By 48 hpi, we found that high ribosome occupancy sites shifted from the N ORF to upstream ORFs, and numerous high ribosome occupancy sites were observed throughout the viral RNAs (**Fig. 1E**). In particular, at 48 hpi, ORF1a and ORF1b translation appeared to be more efficient, considering the low level of mRNA abundance observed by RNA-seq (**Fig. 1E and S7B**). Ribosome occupancy within ORF1a and ORF1b was non-uniform and did not correlate with proteolytic cleavage events occurring within these polyproteins (**Fig. S7A-B**). Ribosome footprints were also observed on antisense transcripts (**Fig. S8**), albeit fairly infrequently and with read length distributions not matching those expected from ribosome protected fragments (**Fig. S2E**).

Similar to other CoVs, SARS-CoV-2 frameshifting is thought to be mediated by the conserved heptanucleotide slippery sequence (UUUAAAC) and a RNA pseudoknot downstream from it spanning nucleotides 13408-13540 (**Fig. 1F**). Of note, ribosome occupancy was fairly low within the frameshifting site but increased immediately following it (**Fig. 1G**), suggesting a relatively high efficiency of frameshifting. Length distribution of reads that mapped to ORF1ab was similar to other virally mapping reads (**Fig. S2F**) and within the expected range of ribosome-protected fragments. Average ribosome density within ORF1b was modestly lower, and comparison of ribosome densities between ORF1a and ORF1b revealed a frameshifting efficiency of %63 (+/- 3%), in line with published reports of frameshifting efficiency with SARS-CoV-2 as well as other coronaviruses (Irigoyen et al., 2016, Dinan et al., 2019, Finkel et al., 2020). In addition, we noted that ribosome density was also depleted ~100 nucleotides upstream of the frameshifting site (**Fig. 1G**). Based on this, we speculate that the pseudoknot structure may sterically hinder translating ribosomes upstream of the frameshifting site or that the RNA structure may extend to upstream sequences.

Kinetics of early translationally regulated events in SARS-CoV-2 replication

To identify early translationally regulated events in SARS-CoV-2 replication, we conducted similar experiments in Vero E6 cells infected at a higher MOI but monitored at earlier times in infection (**Fig. 1A, S1B**). At 2 hpi, only a small fraction of mRNAs was derived from SARS-CoV-2 RNAs, though by 12 hpi, nearly 80% of the total mRNA pool was viral (**Fig. 2A**). Viral RNAs were more abundant in the ribosome bound pool at 2 hpi and by 12 hpi ~50% of the ribosome-protected fragments contained viral sequences (**Fig. 2B**). As before, viral RNAs did not appear to be specifically enriched in the ribosome-bound pool (**Fig. 2B**).

N-derived sequences were the most abundant viral RNA species throughout the infection (**Fig. 2C-G**) and consistent results were obtained from replicate experiments (**Fig. S9-S10**). Analysis of ribosome footprints on viral RNAs at 2 hpi revealed the presence of a high occupancy site (**Fig. 2C, Fig. S11A, and S12A**), which accounted for the majority of ribo-seq reads derived from viral RNAs (**Fig. 2B**). This region, spanning nucleotides 27371-27457 is located between ORF6 and ORF7, is not fully conserved between SARS-CoV-2 and SARS-CoV (**Fig. S13A**), and is predicted to form a structured hairpin loop with high probability (**Fig. S13B**). Reads that mapped to this region displayed a length distribution around 29-34 nt, suggesting that they are authentic ribosome protected fragments rather than aberrant products of PCR or digestion bias. High ribosome occupancy in this region was maintained throughout the infection (**Fig. S13C**) and across biological replicates (**Fig. S11A and S12A**).

Following a high MOI infection, ribosome occupancy on viral RNAs increased significantly by 6 hpi, featuring N and M coding mRNAs constituting as the most frequently translated RNAs (**Fig. 2D, Fig. S11B, and S12B**). Ribosome occupancy across viral RNAs increased further by 12 hpi (**Fig. 2E, S11C and S12C**) and remained high during the remainder of infection (**Fig. 2F, 2G, S11D, S11E, S12D and S12E**). Ribosome footprints were non-uniform with numerous high and low frequency binding sites observed reproducibly across viral RNAs (**Fig. 2C-G, S11, S12**). Of note, the frameshifting element had a generally low ribosome density compared to the surrounding sequences throughout the infection (**Fig. S14A-E**). Ribosome occupancy was low upstream of the frameshifting site (**Fig. S14A-E**), again suggesting the possibility of an alternative RNA structure and/or steric hindrance by the frameshifting element on translating ribosomes. Once again, read length distribution ribo-seq reads mapping to ORF1ab was similar to other virally mapping reads **(Fig. S14F**

vs. Fig. S3B). Comparison of read density distribution between ORF1a and ORF1b indicated a relatively high efficiency of frameshifting ranging from %75 to %100 throughout the course of infection **(Fig. S14G).**

Analogous to SARS-CoV-2, HIV-1 also utilizes -1 ribosomal frameshifting, in this case for generation of the Gag-Pol polyprotein (Jacks et al., 1988, Wilson et al., 1988). HIV-1 frameshifting is regulated by a slippery sequence followed by a structured hairpin loop (Mouzakis et al., 2013, Staple and Butcher, 2005). To compare the frameshifting efficiency of SARS-CoV-2 to HIV-1, we next performed paired ribo-seq and RNA-seq experiments in HIV-1-infected CD4+ T-cells isolated from two independent donors (**Table S5 and S6**). Length distribution of ribo-seq derived reads that mapped to cellular (**Fig. S15A**) and viral (**Fig. S15B**) mRNAs were within the expected range of ribosome-protected fragments. In addition, ribo-seq reads that mapped to cellular mRNAs had a 3-nt periodicity in frame with annotated CDSs (**Fig. S15C**) and were largely depleted off of 3' UTRs (**Fig. S15D**), highlighting the high quality of the ribo-seq experiments.

We found that, in contrast to SARS-CoV-2, ribosome occupancy was high within the HIV-1 frameshifting element (**Fig. S16B**) but dropped substantially 3' to it and remained low throughout the Pol ORF (**Fig. S16A and 16C**). This suggests that ribosomes may pause and accumulate within the frameshifting site but only a small fraction of them continue translating into the Pol ORF, a finding that agrees with prior estimates of low (5-10%) HIV-1 frameshifting efficiency (Biswas et al., 2004, Dulude et al., 2006, Shehu-Xhilaga et al., 2001, Baril et al., 2003, Jacks et al., 1988). Thus, we conclude that programmed ribosomal frameshifting is regulated through distinct mechanisms between HIV-1 and SARS-CoV-2, despite the similar structural elements that regulate this process.

We next tested whether SARS-CoV-2 can utilize alternative translation initiation, which is increasingly recognized as a key post-transcriptional regulatory mechanism (Kwan and Thompson, 2019, James and Smyth, 2018). To do so, ribo-seq experiments were performed as in Fig. 2 but in the presence of harringtonine, which results in the accumulation of ribosomes at translation initiation sites. In addition to accumulation of ribosomes at the canonical start codons, harringtonine treatment resulted in accumulation of ribosomes at alternative translation initiation sites during the course of infection, albeit at generally lower frequencies. For example, at 6 hpi, an internal noncanonical start codon 'UUG' within M ORF was utilized at ~30% of the time, predicted to result in an out-of-frame peptide of 53 amino acids long (**Table S7**). An alternative translation initiation codon 'AGG' at 21868 nt appeared to be utilized within S at 6, 12 and 24 hpi, which would result in a short 18 amino acid peptide (**Table S7**). Finally alternative translation initiation sites were observed within M, resulting in an out-of-frame peptide and a truncated version of M (**Table S7**). Together, these results provide the high resolution map of ribosomes on viral mRNAs during different stages of infection and reveal key sequence and structural elements that may influence SARS-CoV-2 translational program.

Ribo-seq in primary HBECs reveal a similar SARS-CoV-2 translational program

To corroborate these findings in a more relevant cell culture system, we performed ribo-seq studies in primary human bronchial epithelial cells (HBEC) grown at air-liquid interface. Cells inoculated at an MOI of 0.5 were processed for RNA-seq and ribo-seq at 6, 24, 48 and 72 hpi. A parallel set of experiments were done at MOI of 1 and followed during a shorter time course. In contrast to Vero cells, the progression of infection in HBECs was relatively slow and a small percentage of the cells were infected by 24 hpi (not shown). Despite some donor-to-donor variation (as expected from primary cell culture models), SARS-CoV-2 spread was visible by 72 hpi as evident in the presence of numerous infection foci (**Fig. S17A**). By 96 hpi, a large fraction of ciliated cells expressing ACE2 were infected (**Fig. S17B, S17C**). These findings were largely corroborated upon infection of HBECs with a NeonGreen reporter virus (Xie et al., 2020) (**Fig. S17D**). In line with this, the amount of newly synthesized viral RNAs was low at 6 hpi, although by 24 hpi numerous virally derived sequences (as assessed by RNA-seq) were present (**Table S8 and S9**). Similar to experiments done in Vero E6 cells (**Fig. 1 and 2**), the majority of these sequences were derived from subgenomic viral mRNAs coding for N and to a lesser extent upstream ORFs including M, ORF6, ORF7 and ORF8 (**Fig. 3A**). As with previous experiments, length distribution of ribo-seq reads mapping to cellular and viral mRNAs matched the size expected from ribosome-protected fragments (**Fig. S18A**), most ribo-seq reads mapped to CDSs and 5’ UTRs but not 3’ UTRs (**Fig. S18B**) and were enriched in fragments that align to the translated frame (**Fig. S19**), highlighting the high quality of ribo-seq libraries. The lower permissiveness of these cells to infection resulted in few viral RNAs bound to ribosomes at 6 hpi (**Table S8**). Ribosomes bound by viral RNAs were readily detected at 24, 48, and 72 hpi, with N and M ORFs being the most frequently translated (**Fig. 3B-D**). We found distinct accumulation of ribosomes within N, M and ORF1a translation start sites as well as 5’ end of ORF1a (**Fig. 3B-D**). Overall, these results suggest the presence of a similar gene expression cascade in the primary HBECs in comparison to Vero E6 cells.

Inflammatory and innate immune mRNAs are inefficiently translated in SARS-CoV-2 infected cells

Several studies have focused on the transcriptional landscape of innate responses to SARS-CoV-2 (Blanco-Melo et al., 2020, Butler et al., 2020, Menachery et al., 2014, Mitchell et al., 2013, Wilk et al., 2020, Zhou et al., 2020). However, currently there is little evidence as to whether transcriptionally induced mRNAs are actually translated in the setting of a virus that can in principle induce translational arrest (Nakagawa et al., 2016) and ISGs (e.g. IFIT1 and PKR) that can inhibit mRNA translation (Li et al., 2015). Using ribo-seq, we next assessed how cells respond to SARS-CoV-2 infection at a translational level.

Paired RNA-seq and ribo-seq data (for high MOI infections of Vero E6 cells) obtained from independent and reproducible experiments (**Fig. S20**) were analyzed for differential gene expression patterns. As early as 2 hpi, we found transcriptional upregulation of several chemokine ligands (i.e.CXCL1, CXCL3, CXCL8) and transcription factors involved in cell cycle regulation and induction of inflammation (i.e.NR4A3 and EGR3) (**Fig. 4A, S21A, S22A**). In contrast, we noted a general trend in RNA downregulation (**Fig. 4A**), which persisted throughout the infection (**Fig. 4B-C, and S23**). 6 hpi timepoint was also marked by upregulation of chemokine ligands (CXCL1, CXCL3, CXCL8, CXCL11) (**Fig. 4B, S21A, S22A**) and by 12 hpi numerous ISGs (e.g. IFIT family members, MX1, IFI44), IL1A and IFN-λ were also upregulated (**Fig. 4C, S21A, S22A**). Remarkably, the majority of these transcript level changes were not apparent in Ribo-seq data (**Fig. 4D-F and S21A, S22A**), suggesting that mRNAs encoding genes in the host defense responses may not be efficiently translated. Of note, this pattern was not global. For example, EGR1, EGR3 and IFIH1, were induced at equivalent levels both in RNA-seq and ribo-seq experiments (**Fig. S24**). This pattern grossly continued at 24 and 48 hpi, though by 48 hpi upregulated genes were primarily associated with cell death, likely reflecting viral and immune-mediated cytotoxicity (**Fig. S21, S22, S25**).

Time-course gene set enrichment analysis corroborated the differences between transcriptional and translational responses in infected Vero cells. For example, numerous sets of genes involved in chemokine, cytokine and interferon signaling were upregulated at 2 hpi in the RNA-seq data set (**Fig. 5A**), but these changes were not evident in the ribo-seq data set (**Fig. 5B**). Although at later time points both RNA-seq and ribo-seq data sets were enriched in gene sets related to interferon responses, inflammatory responses, IL2 and IL6 signaling, these responses appeared to be lower in magnitude for ribo-seq data, with fewer genes enriched in each family and a significant delay in kinetics (**Fig. 5A-B**). Together, these findings suggest that immune response genes are translationally repressed and their expression significantly delayed in infected cells.

Many of these findings held consistent for the low MOI infections. Analysis of independent and reproducible RNA-seq (**Fig. S26A**) and Ribo-seq (Fig. **S26B**) experiments revealed that transcription factors ATF3 and EGR1, key regulators of inflammatory responses, were upregulated at 24 hpi alongside with numerous chemokine ligands (i.e. CXCL1, CXCL8, CXCL10) and interleukin 6 (**Fig. 6A**). Of note, despite the fact that Vero cells are known to be deficient in type-I IFN production, we noted the upregulation of numerous ISGs (i.e. IFIT1, IFIT2, IFIT3) as well as IFN-lambda at 24 hpi (**Fig. 6A**). The 48 hpi timepoint was marked by upregulation of genes involved in cell cycle regulation and apoptosis (i.e. FOS, NR4A3), as well as inflammatory cytokines such as IL-31 and ISGs including OASL (**Fig. 6B**). In line with our above observations, the great majority of the transcriptionally upregulated genes were not translationally upregulated at 24 hpi (**Fig. 6C**) and 48 hpi (**Fig.6D**). Interleukins IL11 and IL1A stood out as immune-related genes that were translationally upregulated at 24 and 48 hpi, respectively (**Fig. 6C, D**)

Although a small percentage of cells in the primary airway culture system described above were infected, analysis of differentially expressed transcripts revealed significant and consistent trends in gene expression profiles upon infection. For example, we found that gene sets involved in inflammatory response, interferon alpha, interferon gamma, IL2 and

IL6 signaling were upregulated as early as 6 hpi by RNA-seq, despite the lack of observable virus replication (**Fig. S27A**). At 48 hpi, the transcriptional landscape was marked by the upregulation of other sets of genes involved in IL2 and IL6 signaling, inflammation, complement and hypoxia, amongst others (**Fig. S27A**). Many of these responses were tuned down or non-existent in the ribo-seq data set (**Fig. S27B**), suggesting that mRNA translation may similarly be repressed in this more relevant cell culture system.

Comparison of SARS-CoV-2 and host mRNA translation efficiencies

We next assessed the translational efficiency of cellular host response genes in infected cells and how this compared to viral mRNA translation. In mock-infected cells, most cellular mRNAs were translated at levels proportional to their mRNA abundance (**Fig. 7A**). Notable outliers included mRNAs encoding for ribosomal subunits, which were translated less efficiently as observed before (Riba et al., 2019), and DDX25 RNA helicase, which constituted one of the most efficiently translated mRNAs (**Fig. 7A**). The translational efficiency of viral mRNAs was not substantially different than the majority of cellular mRNAs with ORF1AB, S and E mRNAs translated at a modestly higher efficiency and the remainder of viral mRNAs at a lower efficiency than average, a pattern that did not vary with progression of infection (**Fig. 7B-F**). Thus, the high abundance of viral mRNAs, as opposed to a specific regulated mechanism, likely ensures the abundance of viral proteins. Consistent with our earlier observations, we found that the differentially expressed chemokine ligands and ISGs generally were translated less efficiently (**Fig. 7C-D and S14**). Of note numerous cellular genes with unknown functions were translationally upregulated in infected cells (**Fig. 7B-F**).

DISCUSSION

Here we utilized ribosome profiling (ribo-seq) coupled with RNA-seq to study the translational events that regulate viral gene expression and host responses over the course of SARS-CoV-2 infection. SARS-CoV-2 replicates rapidly, with viral RNAs constituting the great majority of the total mRNA pool soon after infection. Our data show that viral mRNA abundance is the main determinant of viral protein expression and SARS-CoV-2 mRNAs sequester ribosomes from the translating pool by competition, simply outnumbering the host counterparts. Notwithstanding certain viral mRNAs (i.e. those encoding S, E and ORF1ab) were translated modestly more efficiently translated than others. While the overall conclusions are similar, another study found that ORF1ab was less efficiently translated compared with other viral mRNAs (Finkel et al., 2020), which we ascribe to possible differences in read depth (with our study having substantially higher read depth within ORF1ab), RNA-seq approaches and infection conditions (5-7 hpi in (Finkel et al., 2020) vs. a more extensive time course analysis done in our study). In addition, we show that ribosome occupancy on viral RNAs is uneven, changes during the course of infection, and alternative translation initiation sites and RNA structural elements may be utilized. Analysis of mRNA translation in infected cells uncovered that inflammatory and innate responses can be dampened by inefficient mRNA translation in SARS-CoV-2 –infected cells. Together, our study provides an in-depth picture of translationally regulated events in SARS-CoV-2 replication and reveal that impairment of host mRNA translation may allow SARS-CoV-2 to evade host immunity.

We observed that, in contrast to HIV-1, SARS-CoV-2 RNA employs a highly efficient frameshifting strategy to facilitate virus replication. Ribosomal frameshifting requires a heptanucleotide slippery sequence and a RNA pseudoknot, generally a H-type, positioned six to eight nucleotides downstream (Giedroc and Cornish, 2009). Multiple models for ribosomal frameshifting posit that the ribosome pauses at the slippery sequence upon encountering the pseudoknot, which is resistant to unwinding (Farabaugh, 1996, Dinman, 2012). While paused, ribosomes either stay in-frame or slip -1 nt before resuming translation. A corollary of this notion is that the stimulatory structure, in turn, enhances frameshifting efficiency by promoting ribosomal pausing. In line with this, we observed low ribosome occupancy in the SARS-CoV-2 frameshifting site (**Fig. 1G and S14**). Notably, ribosome pausing extended 100 nucleotides upstream of the frameshifting site, suggesting an alternative frameshifting structure that includes upstream sequences or steric hindrance imposed by the pseudoknot structure. Ribosome density downstream of the frameshifting site within the ORF1b was remarkably high, suggesting high efficiency of frameshifting in spite of ribosomal pausing.

The behavior of ribosomes was drastically different between the SARS-CoV-2 and HIV-1 frameshifting sites. In contrast to SARS-CoV-2, ribosomes accumulated within the HIV-1 frameshifting element and only a small fraction of them continued into the Pol ORF, suggesting a significantly lower efficiency of frameshifting. We hypothesize that both sequence-specific and structural features contribute to SARS-CoV-2 frameshifting efficiency. It is thought that HIV-1 has a particularly slippery sequence (UUUUUUA) as compared to SARS-CoV-2 (UUUAAAC), which may underlie this difference (Giedroc and Cornish, 2009). In addition, structures downstream of the slippery sequence may have an impact (Plant and Dinman, 2008). For example, the HIV-1 frameshifting element is predicted to have a simpler pseudoknot (Chang et al., 1999, Parkin et al., 1992, Brierley and Dos Ramos, 2006, Huang et al., 2014) or hairpin loop structure (Mouzakis et al., 2013, Staple and Butcher, 2005). In particular, previous studies suggest that frameshifting efficiency positively correlates with the mechanical stability and thermodynamic stability of the pseudoknot and stem loop, respectively (Hansen et al., 2007, Chen et al., 2009, Bidou et al., 1997). In addition, host proteins can also affect frameshifting. Of note, an interferon-stimulated gene (ISG) product, known as C19orf66 (Shiftless), has recently been demonstrated to impair HIV-1 replication through inhibition of HIV-1 programmed frameshifting (Wang et al., 2019). Altogether, our data suggest that SARS-CoV-2 and HIV-1 frameshifting occurs through distinct mechanisms. It remains to be determined how distinct elements within the frameshifting site affect and whether other viral or cellular proteins are involved in modulating the frameshifting efficiencies of these viruses.

SARS-CoV-2 mRNA translation may be regulated by other structural elements. For example, we observed a high ribosome occupancy site that is present throughout the course of infection and located between ORF6 and ORF7 (**Fig. 2C, S13**). This site is computationally predicted to form a structured hairpin loop that may trigger ribosomal pausing during translation of subgenomic viral RNA and thus lead to the observed high ribosome occupancy (**Fig. S8**). Of note, ribosome occupancy within this region fell after harringtonine treatment, suggesting that it may serve a function other than translation initiation (not shown). While the biological role of this RNA structure is not apparent, it may play a role in regulating the relative expression of ORF6 and ORF7 likely within the context of viral subgenomic mRNAs. Other potential functions of this element include co-translational protein folding, protein targeting, or co-translational degradation of both mRNA and nascent peptide following pausing.

In addition, our study demonstrates that alternative, non-canonical translational start sites internal to several viral genes such as S, E and M, can result in truncated isoforms or short peptides (**Table S7**). While their presence still needs to be validated, this raises the question of whether viral protein isoforms may play important biological role during infection. SARS-CoV-2 infection also induced significant increase in utilization of canonical as well as non-canonical translation initiation sites from numerous cellular mRNAs (**Table**

S10), including members of the S100 family with known roles in inflammation (Bettum et al., 2014, Li et al., 2020) and virus replication (Bharadwaj et al., 2013, Liu et al., 2015, Taylor et al., 2018). These findings together emphasize the potential role of translationally regulated events that may help shape viral replication and host responses to pathogens, which may be overlooked in transcriptomics approaches.

Our study provides the first in depth picture of how host cell responses to SARS-CoV-2 are regulated at a post-transcriptional level. This is of utmost importance given that several SARS-CoV proteins have been reported to suppress host translation and that numerous genes involved in innate immunity act to block mRNA translation. Such regulatory events would be completely neglected in transcriptomic screens. In fact, we observed upregulation of proinflammatory chemokines as early as 2 hpi followed by a more delayed induction of ISGs, a finding in line with previous observations in immortalized lung cell lines (Blanco-Melo et al., 2020). However, the increase in transcript abundance did not correlate with higher levels of translation and majority of them appeared to be translated at a low efficiency (**Fig. 7**).

The apparent low translation efficiency of host response mRNAs may be mediated by the SARS-CoV-2 protein nsp1, which was recently reported to associate tightly with the 40S ribosomal subunit as well as non-translating 80S ribosomes to prevent binding of capped mRNA and thus inhibit the formation of the translation initiation complex (Schubert et al., 2020), much like its SARS-CoV counterpart (Narayanan et al., 2015). In addition, there is increasing evidence that ectopic expression of Nsp1 can alter host mRNA translation (Rao et al., 2020). Our study complements these studies and provides the first published evidence on the potential inhibitory effects of Nsp1 on host mRNA translation at biologically relevant infection settings. We cannot rule out that the observed translational suppression may also be contributed by the host's attempt to curb viral replication, including members of the IFIT family with known functions in translation inhibition (Hyde and Diamond, 2015, Fensterl and Sen, 2015, Reynaud et al., 2015, Daffis et al., 2010, Diamond and Farzan, 2013). A further alternative is that the translation of these mRNAs is inherently inefficient due to presence of unique 5' UTR structures. Finally, it is plausible that the relatively lower read depths obtained from ribo-seq libraries may have precluded accurate assessment of differential gene expression changes. However, we think that this is unlikely given the high level of mRNA expression for numerous innate immune genes (based on RNA-seq) and the statistical models utilized herein to assess translational suppression. Notwithstanding, future studies are warranted to empirically test these possibilities and define the mechanism of apparent innate immune suppression.

While COVID-19 pathogenesis is in part due to virus-induced destruction of infected cells, elevated production of inflammatory mediators and the virus-induced immunopathology are thought to play a big role in SARS-CoV-2-induced lung injury (Channappanavar and Perlman, 2017, Perlman and Dandekar, 2005). Our findings suggest that immune responses in actively infected cells may be dampened or delayed for SARS-CoV-2 to efficiently replicate and release viral progeny. As such, it is possible that the elevated levels of inflammatory mediators in vivo is due to infection of immune cell subsets, such as monocytes and macrophages, that are less permissive to SARS-CoV-2 but can sense and respond to infection by secretion of immune modulatory molecules (Jafarzadeh et al., 2020).

Taken together, we provide novel insight into and a rich resource on how translational regulation shapes SARS-CoV-2 replication and host responses. Our finding that induction of inflammatory and innate immune responses can be limited at the level of mRNA translation provides a paradigm shifting mechanism of how SARS-CoV-2 can encounter immune responses. Modulation of viral RNA structures and proteins that regulate mRNA translation will undoubtedly provide a unique avenue for therapeutic development.

ACKNOWLEDGEMENTS: We would like to thank members of the Diamond lab for reagents and support. This work was supported by Washington University startup funds for SBK, R21 AI145669 to SBK and JD, National Science Foundation Graduate Research Fellowship under Grant No. DGE-1745038 to KV, Stephen I. Morse postdoctoral fellowship to MPC, Helen Hay Whitney Foundation postdoctoral fellowship to J.B.C., and the Dorothy R. and Hubert C. Moog Professorship to SLB. All NGS data (48 sets of ribo-seq and 48 sets of matching RNA-seq) are deposited in the GEO database under GSE158930.

AUTHOR CONTRIBUTIONS: MPC, HRV, AH, TH, SGP, JBC conducted the experiments. KT, NL, YL, WY conducted the bioinformatics analysis. HRV and SBK wrote the original manuscript with input from MSD, SLB, JD, JBC.

FIGURE LEGENDS

Figure 1. Ribo-seq reveals uneven ribosome occupancy on SARS-CoV-2 RNAs during low MOI infection. (A) Schematic diagram of Ribo-seq and RNA-seq experiments conducted in this study. Vero E6 cells were infected at 0.1 pfu/cell and cells were processed for RNA-seq and Ribo-seq at 24, 48 and 72 hpi. (B, C) Percentage of RNA-seq (B) and Ribo-seq (C) reads uniquely mapping to SARS-CoV-2 and cellular transcripts at the indicated time points post infection. Individual data points indicate biological replicates. (D, E) Ribo-seq and RNA-seq reads (counts) along the viral genome at 24 hpi (D) and 48 hpi (E). Schematic diagram of SARS2 genome features shown below is co-linear. Red

arrows denote translation initiation sites. (F) Predicted secondary structure of the frameshifting site is depicted. (G) Ribo-seq read counts at 48hpi within the SARS2 frameshifting site. The position of the frameshifting element is indicated with the red rectangle.

Figure 2. Changes in ribosome occupancy on the SARS-CoV-2 genome during high MOI infection. Vero E6 cells were infected at 2 pfu/cell and processed for RNA-seq and Ribo-seq at 2, 6, 12, 24 and 48 hpi. (A, B) Percentage of RNA-seq (A) and Ribo-seq (B) reads uniquely mapping to SARS-CoV-2 and cellular transcripts at the indicated time points post-infection. Individual data points indicate biological replicates. (C-G) Ribo-seq and RNA-seq reads (counts) mapping to the viral genome at 2 hpi (C), 6 hpi (D), 12 hpi (E), 24 hpi (F) and 48 hpi (G) are shown. Schematic diagram of SARS2 genome features illustrated below in co-linear.

Figure 3. Ribo-seq experiments in primary HBEC cultures grown at ALI. HBECs grown at ALI were infected with SARS-CoV-2 at a MOI of 0.5 i.u./cell and processed for RNA-seq at 24 hpi (A) and ribosome profiling at 24 (B), 48 (C) and 72 (D) hpi. Ribo-seq reads (counts, y-axis) along the viral genome (x-axis) is shown. Schematic diagram of SARS2 genome features shown below is co-linear.

Figure 4. Differentially transcribed and translated host genes in SARS-CoV-2-infected cells (high MOI). Vero E6 cells were infected at 2 pfu/cell and processed for RNA-seq at 2 hpi and Ribo-seq at 2 hpi (A, D), 6 hpi (B, E), and 12 hpi (C, F). Heatmaps show the $\log_2$ counts per million mapped reads (cpm) of the top differentially expressed genes (FDR<0.05, fold change>2) derived from two independent experiments. Scale of each graph is shown below.

Figure 5. Expression dynamics of differentially transcribed cellular mRNAs in response to SARS-CoV-2 infection. Time-course gene set analysis (TcGSA) was performed on the RNA-seq (A) and Ribo-seq (B) data derived from the above experiments. The heatmap shows an under (blue) or an over (red) expression for each significant gene set. The numbers next to each gene set indicate a particular subset of genes which trend differently from other genes within the same gene set.

Figure 6. Differentially transcribed and translated host genes in SARS-CoV-2-infected cells (low MOI). Vero E6 cells were infected at 0.1 pfu/cell and cells were processed for RNA-seq (A, B) and Ribo-seq (C, D) at 24 and 48 hpi. Heatmaps show the counts per million mapped reads (cpm) of the top differentially expressed genes (FDR<0.05, fold change>2) derived from two independent experiments. Scale of each graph is shown below.

Figure 7. Comparison of SARS-CoV-2 and host mRNA translation efficiencies. Translation efficiencies of viral and host mRNAs were assessed as described in Materials and Methods. Plots show translational efficiencies of host mRNAs in mock infected cells (A), 2 (B), and 48hpi (C) as these samples all had low or zero viral replication, as well as viral and host mRNAs in infected cells at 6 hpi (C), 12 hpi (D) and 24 hpi (E). Translational efficiencies of key differentially expressed genes derived from RNA-seq and Ribo-seq are represented by orange circles. Reference genes with notably high and low translational efficiencies are represented by blue circles. Viral genes are represented by red circles.

MATERIALS AND METHODS

Chemicals and reagents. Standard laboratory chemicals were obtained from reputable suppliers such as Sigma-Aldrich. Cycloheximide (CHX) was obtained from Sigma, dissolved in ethanol and stored at -20°C. Harringtonine (HT) was purchased from LKT Laboratories, Inc., resuspended in DMSO and stored in aliquots of 2 mg/mL at -20°C.

Plasmids and viruses. A proviral plasmid encoding the full length HIV-1 genome was obtained from NIH AIDS Reagents. HIV-1 stocks were generated by transfection of Human embryonic kidney cell line, HEK293T, with proviral plasmids and collection of cell culture supernatants two days after. Viruses were treated by DNase to avoid plasmid carryover and concentrated by Lenti-X concentrator. HIV-1 stocks were titered on TZM-bl cells by conventional methods. CD4$^+$ T-cells activated for 4-5 days were used for HIV-1 infections. SARS-CoV-2 strain 2019-nCoV/USA-WA1/2020 was obtained from Natalie Thornburg at the Centers for Disease Control and Prevention (CDC), propagated in Vero CCL-81 cells and titrated on Vero E6 cells by plaque-forming assays.

Cells and infections. HEK293T and TZM-bl cells were obtained from ATCC and NIH AIDS Reagent Program respectively and were maintained in Dulbecco's Modified Eagle's Medium (DMEM) (high glucose), supplemented with 10% fetal bovine serum (FBS) in a humidified incubator at 37°C with 5% CO_2. For isolation of primary CD4$^+$ T-cells, buffy coats (from anonymous healthy blood donors from Mississippi Blood Center) were separated by Ficoll and CD4$^+$ T-cells purified using RosetteSep Human CD4+ T-cell enrichment kit (STEMCELL Technologies). CD4$^+$ T-cells cells were maintained in Roswell Park Memorial Institute 1640 medium (RPMI) supplemented with 10% heat-inactivated FBS and L-glutamine. Activation of CD4$^+$ T cells was achieved by addition of 25 U/ml of interleukin-2 (IL-2) and CD4$^+$ T-cell activation Dynabeads (Life Technologies). CD4$^+$ T-cells activated for 4-5 days were used for HIV-1 infections. Vero CCL-81 and Vero E6 were cultured in DMEM supplemented with 10% FBS and 10 mM HEPES pH 7.4. For SARS-CoV-2 infections, Vero E6 cells were incubated with SARS-CoV-2 inoculum in DMEM-supplemented with 2% FBS for an hour in a humidified incubator at 37°C, after which the initial inoculum was removed and replaced by cell culture media.

Primary human bronchial epithelial cells (HBECs) grown at air-liquid interface (ALI). Human airway epithelial cells were isolated from surgical excess of tracheobronchial segments of lungs donated for transplantation as previously described and were exempt from regulation by US Department of Health and Human Services regulation 45 Code of Federal Regulations Part 46 (Horani et al., 2012). Tracheobronchial cells were expanded in culture, seeded on supported membranes (Transwell; Corning, Inc.), and differentiated using ALI conditions as detailed before (You et al., 2002, Horani et al., 2018).

Immunofluorescence. Infected Vero E6 cells and HBECs were fixed with 4% paraformaldehyde for 20 min at room temperature, followed by permeabilization using 0.5% Tween-20 in PBS for 10 min. Cells were blocked with 1% bovine serum albumin (BSA) and 10% FBS in 0.1% Tween-20 PBS (PBST) for 1 h prior to staining with a rabbit polyclonal anti SARS-CoV-2 nucleocapsid antibody (Sino Biological Inc. catalog # 40588-T62) diluted 1:500 and incubated overnight at 4°C. The following day, cells were stained with an Alexa Fluor 488-conjugated goat anti-rabbit secondary antibody (Invitrogen) at 1:1000 dilution, counter-stained with DAPI and imaged by microscopy.

RNA in situ hybridization. Primary-culture human airway epithelial cells were fully differentiated at air-liquid interface on supported plastic membranes (Transwell, Corning). Cells were fixed by immersion of the Transwell membrane in methanol:acetone (50:50%

volume) at -20 °C for 20 min followed by 4% paraformaldehyde at room temperature for 15 min. Cells were washed three times with phosphate buffered saline (PBS) and stored at 4 °C. Prior to probing for vRNA, membranes containing cells were cut from plastic supports, divided into 4 pieces, and placed in a fresh 48-well plate. RNA detection was performed using the manufacturer protocol for RNAscope fluorescent in situ hybridization (RNAscope Multiplex Fluorescent v2 Assay kit, Advanced Cell Diagnostics). Briefly, cells on membranes were treated with 3% hydrogen peroxide for 10 min at room temperature, washed with distilled water, then treated with protease III solution, diluted 1:15 in PBS, for 10 min in a humidified hybridization oven at 40 °C. The cells were then washed with PBS and incubated for 2 hr at 40 °C with manufacturer designed anti-sense probes specific for SARS-CoV-2 positive strand S gene encoding the spike protein (RNAscope Probe-V-nCoV2019-S, cat# 848561) or ORF1ab (RNAscope Probe-V-nCoV2019-orf1ab-O2-sense-C2 cat # 854851-C2). The probes were visualized according to the manufacturers' instructions by incubation with RNAscope amplifiers, horseradish peroxidase, and fluorescent label (Opal fluorophores, Perkin-Elmer). Membranes were mounted on glass slides using anti-fade medium containing DAPI (Fluoroshield, Sigma-Aldrich). Images were obtained using a 5000B Leica microscope equipped with a charge-coupled device camera (Retiga 200R) interfaced with QCapture Pro software (Q Imaging).

Ribosome profiling. Ribosome profiling (Ribo-seq) was performed as described before with the following modifications (Ingolia et al., 2009, Ingolia et al., 2012). Mock- and HIV-1- or SARS-CoV-2-infected cells were treated with complete cell culture media supplemented with 0.1 mg/mL CHX for 1 min at room temperature followed by one round of wash in ice-cold PBS supplemented with 0.1 mg/mL CHX. Cells were lysed in 1X mammalian polysome lysis buffer (20 mM Tris·HCl (pH 7.4), 150 mM NaCl, 5 mM $MgCl_2$, 1% Triton X-100, 0.1% NP-40, 1 mM DTT, 10 units of DNase I, with 0.1 mg/mL CHX). The cells were then triturated by repeated pipetting and incubated with lysis buffer for at least 20 min to ensure virus inactivation. Lysates were centrifuged for 10 min at ≥20,000 g at 4°C for clarification. The supernatants were split into multiple aliquots, with SDS added to one aliquot to a final concentration of 1% for downstream RNA-seq sample preparation, and flash frozen in a 70% ethanol/dry ice bath or directly placed at -80°C. Lysates were treated with RNase I (5U/OD_{260}) and ribosome-protected fragments were isolated via centrifugation through Microspin S-400 HR columns (GE Healthcare) and purified using the RNA Clean and Concentrator kit (Zymo Research). Recovered ribosome-bound fragments (RBFs) are then subjected to rRNA depletion using RiboZero beads from the TruSeq Stranded Total RNA Library Prep Gold kit (Illumina) and purified using Zymo RNA Clean and Concentrator kit. Fragments were then end-labeled with γ-^{32}P-ATP using T4 polynucleotide kinase (NEB), separated on 15% TBE-Urea gels and visualized by autoradiography. RNA fragments of ~30 nt were excised from the gels and purified as detailed before in 400 μL of 0.4 M NaCl supplemented with 4 μL SUPERaseIN. 3' and 5' adapters were sequentially ligated as in a previously described protocol (Kutluay et al., 2014, Kutluay and Bieniasz, 2016), reverse transcribed and PCR amplified. Libraries were then sequenced on HiSeq-2000 or NextSeq 500 platforms (Illumina) at the Genome Technology Access Center or the Edison Family Center for Genome Sciences & Systems Biology, respectively, at Washington University School of Medicine. All ribo-seq and RNA-seq data were deposited on GEO database under GSE158930.

RNA-seq. An aliquot of cell lysates harvested from ribosome profiling (Ribo-seq) experiments above was processed in parallel for RNA-seq using TruSeq Stranded mRNA library prep (Illumina) following extraction using Zymo RNA-Clean and Concentrator (5) kit. RNA-seq libraries were constructed using TruSeq RNA single-index adapters and deep sequenced as above at Washington University in St. Louis.

Data analysis. All of the data analysis pipelines used in this study are deposited to GitHub under kutluaylab. Below we detail the salient steps of data analyses:

Mapping. Generated RNA-seq and Ribo-seq data were analyzed by publicly available software and custom scripts. In brief, for Ribo-seq, reads were separated based on barcodes and the adapters trimmed using BBDuk (http://jgi.doe.gov/data-and-tools/bb-tools/) and FastX Toolkit (http://hannonlab.cshl.edu/fastx_toolkit/). The resulting reads were mapped to the viral genome/transcriptome using the Bowtie aligner (Langmead et al., 2009) (mapping criteria -v 1, -m 10), and to the African green monkey (AGM) genome (*Chlorocebus sabaeus*) in STAR (Dobin et al., 2013) (mapping criteria FilterMismatchNoverLmax 0.04). For AGM alignments, reads were first mapped to rRNA to remove any rRNA-derived reads not completely removed by depletion kits and to the SARS-CoV-2 genome to remove virally derived reads. The remaining reads were then mapped to the AGM genome. RNA-seq reads were similarly mapped to the viral and AGM genomes using STAR, although the rRNA alignment step was omitted. For AGM alignments, mapped reads were annotated using the featureCounts package and GTF files freely available from NCBI and Ensembl.

Statistical Analysis: Differential gene expression analysis was carried out using the featureCounts output files via the edgeR package (Robinson et al., 2010), available from Bioconductor. Considering that virally derived sequences quickly dominated the host mRNA pool, for differential gene expression of host mRNAs, library sizes were normalized relative to reads that map only to host mRNAs. Efforts in this area focused on determining upregulated genes using individual Ribo-seq and RNA-seq experiments, as well as the analysis of $\log_2$-fold change differences between Ribo-seq and RNA-seq to discover translationally regulated genes. These same files and packages were also used to generate quality control plots and graphics highlighting differentially expressed genes. The calculation of translational efficiency involved normalizing counts to account for library size in edgeR to generate log2 counts-per-million ($\log_2$CPM) estimates for each gene in Ribo-seq and RNA-seq, and subtracting log2CPM RNA-seq from $\log_2$CPM Ribo-seq to provide an estimate of the difference in expression level between Ribo-seq and RNA-seq for a given gene.

Additionally, the R package TcGSA was used to determine individual host genes and gene sets differentially regulated over time (Hejblum et al., 2015). The normalized gene counts at each time-point were provided as input, along with the 'hallmark' Gene Matrix file containing annotated sets of processes and associated genes, downloaded from GSEA (Subramanian et al., 2005, Mootha et al., 2003). As output, TcGSA provides clusters of genes within each gene set, which follow particular trends. From these clusters, individual genes differentially regulated over time were extracted and plotted as heatmaps in R.

Downstream analysis of sets of differential genes involved the use of goseq (Young et al., 2010) and KEGGREST R packages (Tenenbaum, 2020). Annotations of 5'UTRs, CDSs and 3'UTRs were retrieved and repetitive low-complexity elements were removed. The R package riboWaltz (Lauria et al., 2018) was utilized to determine the location of ribosomal P-sites with respect to the 5' and 3' end of reads, as well as illustrating triplet periodicity and determining the percentage of reads within each frame in CDS and UTR . Finally, the metagene R package (Beauparlant, 2020) was applied to generate an aggregate analysis of ribosomal density downstream of start codons and upstream of stop codons in the corresponding genome.

Alternative TIS sites in both host and viral reads were found using the Ribo-TISH package (Zhang et al., 2017). For viral TIS, analysis was carried out in the 'predict' mode comparing samples mock-treated or treated with harringtonine at each timepoint (with replicates). This was replicated for host analysis, although with the additional step of analysis in the 'diff' mode to predict TIS differentially regulated between infected and uninfected cells.

Viral Counts: Viral read density plots were generated using the SAM file from viral genome alignment. The SAMtools (Li et al., 2009) package was used to create an mpileup file containing information about the read density, strandedness, mapping quality, and nucleotide identity at each position. Custom scripts (deposited at GitHub under kutluaylab) then were utilized to create files providing only the nucleotide identity and number of counts at each position for both sense and antisense reads. These were then visualized by scripts written in R.

As SARS-CoV-2 generates chimeric subgenomic mRNAs (sgRNAs) in addition to its genomic RNA (gRNA), featureCounts could not be used to accurately estimate viral gene counts from RNASeq due to the presence of nested 3' sequences. Therefore, in order to visualize and enumerate such chimeric sequences the BWA aligner (Li and Durbin, 2009) was used in 'mem' mode on viral RNASeq reads. After generating this alignment using the default parameters and same reference SARS-CoV-2 FASTA file as above, chimeric reads were isolated by searching for all reads containing the 'SA' tag and the SARS TRS sequence, 'AAACGAAC'. SARS-CoV-2 gRNAs were extracted by searching for all reads containing the first 15-20 bases of the ORF1A coding sequence (CDS), as these sequences would only be present in full-length SARS-CoV-2 genomes. This provided the sequences and alignment locations of the chimeric and genomic reads, which were then visualized using R. For sgRNAs, the viral gene corresponding to each transcript was determined by locating the CDS with the nearest downstream start site. This data, together with the number of gRNAs was used to calculate relative percentages of viral transcripts and, together with the total number of mapped viral reads, allowed for the tabulation of viral gene counts at each time point. For ribosome profiling data, featureCounts was used to enumerate the number of viral reads, as ribosomes only translate the first gene on each transcript and so footprints from nested 3' gene were low enough to be negligible.

SUPPLEMENTARY FIGURE LEGENDS

Figure S1. SARS-CoV-2 infection of Vero E6 cells (Supplemental to Figure 1 and Figure 2). Vero cells were infected at an MOI of 0.1 pfu/cell (A) or 2 pfu/cell (B). Infected cells were fixed at the indicated time points post-infection and stained using an antibody against the viral N protein and visualized by microscopy.\

Figure S2. Quality control of Ribo-seq libraries derived from Vero E6 cells infected with SARS-CoV-2 at a low MOI (Supplemental to Figure 1). Vero E6 cells infected as in Fig. 1A at an MOI of 0.1 pfu/cell were processed for ribo-seq as detailed in Materials and Methods. (A) Length distribution of ribo-seq-derived reads mapping to the African green monkey (AGM) transcriptome are shown from independent replicates. (B) Length distribution of ribo-seq-derived reads mapping to SARS-CoV-2 genome. (C) Number or reads mapping to 5'UTR, CDS and 3' UTRs of annotated AGM genes in matching RNA-seq and ribo-seq libraries are shown. (D) Meta-profiles showing the periodicity of ribosomes along the AGM transcripts at the genome-wide scale from independent replicate samples. (E, F) Length distribution of ribo-seq-derived reads mapping to anti-sense SARS-CoV-2 transcripts (E) or SARS-CoV-2 ORF1ab region (F).

Figure S3. Length distribution of ribo-seq reads derived from Vero E6 cells infected with SARS-CoV-2 at a high MOI (Supplemental to Figure 2). Vero E6 cells infected with SARS-CoV-2 as in Fig. 1A at an MOI of 2 pfu/cell were processed for ribo-seq as detailed in Materials and Methods. (A) Length distribution of ribo-seq-derived reads mapping to the African green monkey (AGM) transcriptome are shown from independent replicates. (B, C) Length distribution of ribo-seq-derived reads mapping to SARS-CoV-2 genome (B) or anti-sense SARS-CoV-2 transcripts (C) from independent experiments are shown.

Figure S4. Ribo-seq-derived reads map to 5'UTRs and CDSs but are depleted of 3'UTRs (Supplemental to Figure 2). Vero E6 cells infected with SARS-CoV-2 as in Fig. 1A at an MOI of 2 pfu/cell were processed for ribo-seq and RNA-seq as detailed in Materials and Methods. Reads mapping to 5'UTRs, CDSs and 3'UTRs of the AGM transcriptome are depicted for the indicated samples.

Figure S5. Metaprofiles and P-site analyses of ribo-seq reads derived from Vero E6 cells infected at a MOI of 2 pfu/cell (Supplemental to Figure 2). Meta-profiles showing the periodicity of ribosomes along the AGM transcripts at the genome-wide scale from independent ribo-seq libraries.

Figure S6. RNA-seq on sense and antisense SARS-CoV-2 transcripts during low MOI infection (Supplemental to Figure 1). Data derived from experiments described in Figure 1 and a replicate experiment were plotted to demonstrate the number of reads that map to sense vs. antisense transcripts at 24 (A) and 48 (B) hpi. Schematic diagram of SARS-CoV-2 genome features shown below is co-linear.

Figure S7. Ribosome occupancy on the SARS-CoV-2 genome during low MOI infection (Supplemental to Figure 1). Vero E6 cells were infected at 0.1 pfu/cell and cells were processed for RNA-seq and Ribo-seq as in Figure 1. Ribo-seq and RNA-seq reads (counts) mapping to the first 20000 nucleotides (ORF1ab) of the viral genome at 24 (A) and 48 (B) hpi with constituent non-structural proteins (NSPs) shown below is co-linear.

Figure S8. Ribosome occupancy on sense and antisense SARS-CoV-2 transcripts during low MOI infection (Supplemental to Figure 1). Ribo-seq data derived from the two independent experiments described in Figure 1 were plotted to demonstrate the number of reads mapping to sense and antisense transcripts at 24 (A, C) and 48 (B, D) hpi. Schematic diagram of SARS2 genome features shown below is co-linear.

Figure S9. RNA-seq on sense and antisense SARS-CoV-2 transcripts during high MOI infection (Supplemental to Figure 2). RNA-seq data derived from experiments described in Figure 1 were plotted to demonstrate the number of reads that map to sense and. antisense transcripts at 2 hpi (A), 6 hpi (B), 12 hpi (C), 24 hpi (D) and 48 hpi (E). Schematic diagram of SARS2 genome features shown below is co-linear.

Figure S10. Reproducibility of RNA-seq experiments (Supplemental to Figure 2). RNA-seq data derived from a replicate experiment described in Figure 1 were plotted to demonstrate the number of reads that map to sense vs. antisense transcripts at 2 hpi (A), 6 hpi (B), 12 hpi (C), 24 hpi (D) and 48 hpi (E). Schematic diagram of SARS2 genome features shown below is co-linear.

Figure S11. Ribosome occupancy on sense and antisense SARS-CoV-2 transcripts during high MOI infection (Supplemental to Figure 2). Ribo-seq data derived from experiments described in Figure 1 were plotted to demonstrate the number of reads that map to sense vs. antisense transcripts at 2 hpi (A), 6 hpi (B), 12 hpi (C), 24 hpi (D) and 48 hpi (E). Schematic diagram of SARS2 genome features shown below is co-linear.

Figure S12. Reproducibility of Ribo-seq experiments (Supplemental to Figure 2). Ribo-seq data derived from a replicate experiment described in Figure 1 were plotted to demonstrate the number of reads that map to sense vs. antisense transcripts at 2 hpi (A), 6 hpi (B), 12 hpi (C), 24 hpi (D) and 48 hpi (E). Schematic diagram of SARS2 genome features shown below is co-linear.

Figure S13. Properties of the high ribosome occupancy site located between 27371-27457 nt (supplemental to Figure 2). (A) Sequence homology of the high ribosome occupancy site between SARS-CoV-2 27371-27457nts and SARS-CoV (27243-27336). (B) Predicted secondary structure of the SARS-CoV-2 sequence at 27371-27457nts using RNAstructure. (C) Ribosome occupancy surrounding nucleotides 27371-27457 at the indicated time points post-infection.

Figure S14. Ribosome occupancy remains low within the SARS-CoV-2 frameshifting site throughout infection (supplemental to Figure 2). (A-E) Ribosome occupancy surrounding and within the frameshifting site at the indicated time points post-infection (derived from Ribo-seq experiments in Figure 2) is shown. Red bars indicate the position of the frameshifting element. (F) Length distribution of ribo-seq-derived reads mapping to SARS-CoV-2 ORF1ab. (G) ORF1arameshifting efficiency of SARS-CoV-2 throughout the course of infection.

Figure S15. Quality control of Ribo-seq libraries derived from primary CD4+ T-cells infected with HIV-1 (Supplemental to Figure 2). CD4+ T-cells isolated from two independent donors infected HIV-1 were processed for ribo-seq as detailed in Materials and Methods. Length distribution of ribo-seq-derived reads mapping to the human transcriptome (A) and HIV-1 genome (B) are shown for independent replicates. (C) Meta-profiles showing the periodicity of ribosomes along the human transcripts at the genome-wide scale from independent replicate samples. (D) Number or reads mapping to 5'UTR, CDS and 3' UTRs of annotated human genes in matching RNA-seq and ribo-seq libraries are shown.

Figure S16. RIbo-seq in HIV-1-infected cells reveals structural elements that regulate translation (supplemental to Figure 2). Primary CD4+ T-cells were infected with HIV-1_{NL4-3}/VSV-G at an MOI of 2 and infected cells processed for RNA-seq and Ribo-seq at 24 hpi. (A) Ribo-seq and RNA-seq reads (counts) mapping to the HIV-1 genome is shown. Schematic diagram of HIV-1 genome features shown below is co-linear. (B) Secondary structure prediction of the HIV-1 ribosome frameshifting element is shown. (C) Ribosome occupancy within the frameshifting site is shown.

Figure S17. SARS-CoV-2 infection of primary HBECs grown at ALI (supplemental to Figure 3). (A) Primary HBEC cultures were infected with SARS-CoV-2 at an MOI of 0.5 pfu/cell and fixed at 72 hpi. Cells were probed with anti-spike (anti-S) and anti-nucleoprotein (anti-N) antibodies and imaged by microscopy. (B, C) Primary HBEC cultures were infected with SARS-CoV-2 at an MOI of 1 pfu/cell and fixed at 96 hpi. Cells were probed with RNAScope probes against sense- and anti-sense SARS-CoV-2 transcripts, and imaged by microscopy with a 4X (B) or 20X objective (C). (D) Primary

HBEC cultures were infected with SARS-CoV-2-NeonGreen and imaged live during the course of infection at the indicated time points.

Figure S18. Quality of ribo-seq experiments from SARS-CoV-2-infected primary HBECs grown at ALI (supplemental to Figure 3). Primary HBEC cultures were infected with SARS-CoV-2 at an MOI of 0.5 or MOI of 1 pfu/cell as in Figure 3 and processed for ribo-seq at the indicated times post-infection. (A, B) Length distribution of ribo-seq-derived reads mapping to the human transcriptome (A) and SARS-CoV-2 genome (B) are shown. (C) Number or reads mapping to 5'UTR, CDS and 3' UTRs of annotated human genes in matching RNA-seq and ribo-seq libraries are shown.

Figure S19. Metaprofiles and P-site analyses of ribo-seq reads derived from SARS-CoV-2-infected primary HBEC cells (Supplemental to Figure 3). Meta-profiles showing the periodicity of ribosomes along the human transcripts at the genome-wide scale from independent ribo-seq libraries derived from primary HBECs infected at the indicated MOIs and times post-infection.

Figure S20. Reproducibility of RNA-seq and ribo-seq data sets (supplemental to Figure 4). (A) Correlation of $\log_2$(counts per million mapped reads) for each gene derived from RNA-seq experiments is shown. **(B)** Correlation of $\log_2$ counts per million mapped reads for each gene derived from ribo-seq experiments is shown.

Figure S21. Time-course analysis of differentially expressed genes in response to SARS-CoV-2 infection (Supplemental to Figure 4). Differentially expressed genes across different time points from Figure 4 were plotted to demonstrate the time-course progression of differential gene expression in RNA-seq and ribo-seq data sets. Data show the $\log_2$(fold-change) values of genes that are up- or down-regulated greater than 2-fold with FDR<0.05.

Figure S22. Time-course analysis of differentially expressed genes in response to SARS-CoV-2 infection (Supplemental to Figure 4). Log_2(cpm) values of differentially expressed genes from Figure 4 are plotted for each experiment.

Figure S23. SARS-CoV-2 infection induces a general decrease in host mRNA expression (high MOI, supplemental to Figure 4). Vero E6 cells were infected at 2 pfu/cell and cells were processed for RNA-seq. Volcano plots show the $\log_2$ fold-change (x-axis) vs. significance (-log(Pvalue), y-axis) of host genes at 2 hpi (A), 6 hpi (B), 12 hpi (C), 24 hpi (D) and 48 hpi (E). Top differentially expressed genes (FDR<0.05, fold change>2) are indicated by blue dots.

Figure S24. SARS-CoV-2 infection results in lower translation rates for mRNAs coding for immune responses (supplemental to Figure 4). Expression levels (fold change over mock) of select immune-related mRNAs that were significantly upregulated in RNA-seq data set were compared to expression levels derived from ribo-seq data set.

Figure S25. Differentially transcribed and translated host genes in SARS-CoV-2-infected cells (supplemental to Figure 4). Vero E6 cells were infected at 2 pfu/cell and processed for RNA-seq at 2 hpi and Ribo-seq at 24 hpi (A, C) and 48 hpi (B, D). Heatmaps show the $\log_2$ counts per million mapped reads (cpm) of the top differentially expressed genes (FDR<0.05, fold change>2) derived from two independent experiments. Scale of each graph is shown below.

Figure S26. Reproducibility of RNA-seq and ribo-seq data sets (supplemental to Figure 7). (A) Correlation of $\log_2$(counts per million mapped reads) for each gene derived from RNA-seq experiments (low MOI) is shown. **(B)** Correlation of $\log_2$ counts per million mapped reads for each gene derived from ribo-seq experiments (low MOI) is shown.

Figure S27. Transcriptional responses of HBECs to SARS-CoV-2. HBECs grown at ALI were infected with SARS-CoV-2 at a MOI of 0.5 i.u./cell and processed for RNA-seq (A) and ribo-seq (B) at 6, 24 and 48 hpi. Data were analyzed for trends in gene set enrichment over the period of infection.

REFERENCES

BARIL, M., DULUDE, D., GENDRON, K., LEMAY, G. & BRAKIER-GINGRAS, L. 2003. Efficiency of a programmed -1 ribosomal frameshift in the different subtypes of the human immunodeficiency virus type 1 group M. *RNA,* 9**,** 1246-53.

BEAUPARLANT, C. J., LAMAZE, F.C., SAMB, R., LIPPENS, C., DESCHENES, A.L., DROIT, A. 2020. metagene: A package to produce metagene plots. R package version 2.20.0. .

BETTUM, I. J., VASILIAUSKAITE, K., NYGAARD, V., CLANCY, T., PETTERSEN, S. J., TENSTAD, E., MAELANDSMO, G. M. & PRASMICKAITE, L. 2014. Metastasis-associated protein S100A4 induces a network of inflammatory cytokines that activate stromal cells to acquire pro-tumorigenic properties. *Cancer Lett,* 344**,** 28-39.

BHARADWAJ, A., BYDOUN, M., HOLLOWAY, R. & WAISMAN, D. 2013. Annexin A2 heterotetramer: structure and function. *Int J Mol Sci,* 14**,** 6259-305.

BIDOU, L., STAHL, G., GRIMA, B., LIU, H., CASSAN, M. & ROUSSET, J. P. 1997. In vivo HIV-1 frameshifting efficiency is directly related to the stability of the stem-loop stimulatory signal. *RNA,* 3**,** 1153-8.

BISWAS, P., JIANG, X., PACCHIA, A. L., DOUGHERTY, J. P. & PELTZ, S. W. 2004. The human immunodeficiency virus type 1 ribosomal frameshifting site is an invariant sequence determinant and an important target for antiviral therapy. *J Virol,* 78**,** 2082-7.

BLANCO-MELO, D., NILSSON-PAYANT, B. E., LIU, W. C., UHL, S., HOAGLAND, D., MOLLER, R., JORDAN, T. X., OISHI, K., PANIS, M., SACHS, D., WANG, T. T., SCHWARTZ, R. E., LIM, J. K., ALBRECHT, R. A. & TENOEVER, B. R. 2020.

Imbalanced Host Response to SARS-CoV-2 Drives Development of COVID-19. *Cell,* 181**,** 1036-1045 e9.

BRIERLEY, I. & DOS RAMOS, F. J. 2006. Programmed ribosomal frameshifting in HIV-1 and the SARS-CoV. *Virus Res,* 119**,** 29-42.

BUTLER, D. J., MOZSARY, C., MEYDAN, C., DANKO, D., FOOX, J., ROSIENE, J., SHAIBER, A., AFSHINNEKOO, E., MACKAY, M., SEDLAZECK, F. J., IVANOV, N. A., SIERRA, M., POHLE, D., ZIETZ, M., GISLADOTTIR, U., RAMLALL, V., WESTOVER, C. D., RYON, K., YOUNG, B., BHATTACHARYA, C., RUGGIERO, P., LANGHORST, B. W., TANNER, N., GAWRYS, J., MELESHKO, D., XU, D., STEEL, P. A. D., SHEMESH, A. J., XIANG, J., THIERRY-MIEG, J., THIERRY-MIEG, D., SCHWARTZ, R. E., IFTNER, A., BEZDAN, D., SIPLEY, J., CONG, L., CRANEY, A., VELU, P., MELNICK, A. M., HAJIRASOULIHA, I., HORNER, S. M., IFTNER, T., SALVATORE, M., LODA, M., WESTBLADE, L. F., CUSHING, M., LEVY, S., WU, S., TATONETTI, N., IMIELINSKI, M., RENNERT, H. & MASON, C. E. 2020. Shotgun Transcriptome and Isothermal Profiling of SARS-CoV-2 Infection Reveals Unique Host Responses, Viral Diversification, and Drug Interactions. *bioRxiv*.

CHANG, S. Y., SUTTHENT, R., AUEWARAKUL, P., APICHARTPIYAKUL, C., ESSEX, M. & LEE, T. H. 1999. Differential stability of the mRNA secondary structures in the frameshift site of various HIV type 1 viruses. *AIDS Res Hum Retroviruses,* 15**,** 1591-6.

CHANNAPPANAVAR, R. & PERLMAN, S. 2017. Pathogenic human coronavirus infections: causes and consequences of cytokine storm and immunopathology. *Semin Immunopathol,* 39**,** 529-539.

CHEN, G., CHANG, K. Y., CHOU, M. Y., BUSTAMANTE, C. & TINOCO, I., JR. 2009. Triplex structures in an RNA pseudoknot enhance mechanical stability and increase efficiency of -1 ribosomal frameshifting. *Proc Natl Acad Sci U S A,* 106**,** 12706-11.

DAFFIS, S., SZRETTER, K. J., SCHRIEWER, J., LI, J., YOUN, S., ERRETT, J., LIN, T. Y., SCHNELLER, S., ZUST, R., DONG, H., THIEL, V., SEN, G. C., FENSTERL, V., KLIMSTRA, W. B., PIERSON, T. C., BULLER, R. M., GALE, M., JR., SHI, P. Y. & DIAMOND, M. S. 2010. 2'-O methylation of the viral mRNA cap evades host restriction by IFIT family members. *Nature,* 468**,** 452-6.

DE WIT, E., VAN DOREMALEN, N., FALZARANO, D. & MUNSTER, V. J. 2016. SARS and MERS: recent insights into emerging coronaviruses. *Nat Rev Microbiol,* 14**,** 523-34.

DIAMOND, M. S. & FARZAN, M. 2013. The broad-spectrum antiviral functions of IFIT and IFITM proteins. *Nat Rev Immunol,* 13**,** 46-57.

DINAN, A. M., KEEP, S., BICKERTON, E., BRITTON, P., FIRTH, A. E. & BRIERLEY, I. 2019. Comparative Analysis of Gene Expression in Virulent and Attenuated Strains of Infectious Bronchitis Virus at Subcodon Resolution. *J Virol,* 93.

DINMAN, J. D. 2012. Mechanisms and implications of programmed translational frameshifting. *Wiley Interdiscip Rev RNA,* 3**,** 661-73.

DOBIN, A., DAVIS, C. A., SCHLESINGER, F., DRENKOW, J., ZALESKI, C., JHA, S., BATUT, P., CHAISSON, M. & GINGERAS, T. R. 2013. STAR: ultrafast universal RNA-seq aligner. *Bioinformatics,* 29**,** 15-21.

DULUDE, D., BERCHICHE, Y. A., GENDRON, K., BRAKIER-GINGRAS, L. & HEVEKER, N. 2006. Decreasing the frameshift efficiency translates into an equivalent reduction of the replication of the human immunodeficiency virus type 1. *Virology,* 345**,** 127-36.

FARABAUGH, P. J. 1996. Programmed translational frameshifting. *Microbiol Rev,* 60**,** 103-34.

FENSTERL, V. & SEN, G. C. 2015. Interferon-induced Ifit proteins: their role in viral pathogenesis. *J Virol,* 89**,** 2462-8.

FINKEL, Y., MIZRAHI, O., NACHSHON, A., WEINGARTEN-GABBAY, S., MORGENSTERN, D., YAHALOM-RONEN, Y., TAMIR, H., ACHDOUT, H., STEIN, D., ISRAELI, O., BETH-DIN, A., MELAMED, S., WEISS, S., ISRAELY, T., PARAN, N., SCHWARTZ, M. & STERN-GINOSSAR, N. 2020. The coding capacity of SARS-CoV-2. *Nature*.

GARCIA-MIRANDA, P., BECKER, J. T., BENNER, B. E., BLUME, A., SHERER, N. M. & BUTCHER, S. E. 2016. Stability of HIV Frameshift Site RNA Correlates with Frameshift Efficiency and Decreased Virus Infectivity. *J Virol,* 90**,** 6906-6917.

GIEDROC, D. P. & CORNISH, P. V. 2009. Frameshifting RNA pseudoknots: structure and mechanism. *Virus Res,* 139**,** 193-208.

HANSEN, T. M., REIHANI, S. N., ODDERSHEDE, L. B. & SORENSEN, M. A. 2007. Correlation between mechanical strength of messenger RNA pseudoknots and ribosomal frameshifting. *Proc Natl Acad Sci U S A,* 104**,** 5830-5.

HEJBLUM, B. P., SKINNER, J. & THIEBAUT, R. 2015. Time-Course Gene Set Analysis for Longitudinal Gene Expression Data. *PLoS Comput Biol,* 11**,** e1004310.

HORANI, A., DRULEY, T. E., ZARIWALA, M. A., PATEL, A. C., LEVINSON, B. T., VAN ARENDONK, L. G., THORNTON, K. C., GIACALONE, J. C., ALBEE, A. J., WILSON, K. S., TURNER, E. H., NICKERSON, D. A., SHENDURE, J., BAYLY, P. V., LEIGH, M. W., KNOWLES, M. R., BRODY, S. L., DUTCHER, S. K. & FERKOL, T. W. 2012. Whole-exome capture and sequencing identifies HEATR2 mutation as a cause of primary ciliary dyskinesia. *Am J Hum Genet,* 91**,** 685-93.

HORANI, A., USTIONE, A., HUANG, T., FIRTH, A. L., PAN, J., GUNSTEN, S. P., HASPEL, J. A., PISTON, D. W. & BRODY, S. L. 2018. Establishment of the early cilia preassembly protein complex during motile ciliogenesis. *Proc Natl Acad Sci U S A,* 115**,** E1221-E1228.

HUANG, C., LOKUGAMAGE, K. G., ROZOVICS, J. M., NARAYANAN, K., SEMLER, B. L. & MAKINO, S. 2011. SARS coronavirus nsp1 protein induces template-dependent endonucleolytic cleavage of mRNAs: viral mRNAs are resistant to nsp1-induced RNA cleavage. *PLoS Pathog,* 7**,** e1002433.

HUANG, J., HUME, A. J., ABO, K. M., WERDER, R. B., VILLACORTA-MARTIN, C., ALYSANDRATOS, K. D., BEERMANN, M. L., SIMONE-ROACH, C., OLEJNIK, J., SUDER, E. L., BULLITT, E., HINDS, A., SHARMA, A., BOSMANN, M., WANG, R., HAWKINS, F., BURKS, E. J., SAEED, M., WILSON, A. A., MUHLBERGER, E. & KOTTON, D. N. 2020. SARS-CoV-2 Infection of Pluripotent Stem Cell-derived Human Lung Alveolar Type 2 Cells Elicits a Rapid Epithelial-Intrinsic Inflammatory Response. *bioRxiv*.

HUANG, X., YANG, Y., WANG, G., CHENG, Q. & DU, Z. 2014. Highly conserved RNA pseudoknots at the Gag-Pol junction of HIV-1 suggest a novel mechanism of -1 ribosomal frameshifting. *RNA,* 20**,** 587-93.

HYDE, J. L. & DIAMOND, M. S. 2015. Innate immune restriction and antagonism of viral RNA lacking 2-O methylation. *Virology,* 479-480**,** 66-74.

INGOLIA, N. T., BRAR, G. A., ROUSKIN, S., MCGEACHY, A. M. & WEISSMAN, J. S. 2012. The ribosome profiling strategy for monitoring translation in vivo by deep sequencing of ribosome-protected mRNA fragments. *Nat Protoc,* 7**,** 1534-50.

INGOLIA, N. T., GHAEMMAGHAMI, S., NEWMAN, J. R. & WEISSMAN, J. S. 2009. Genome-wide analysis in vivo of translation with nucleotide resolution using ribosome profiling. *Science,* 324**,** 218-23.

IRIGOYEN, N., FIRTH, A. E., JONES, J. D., CHUNG, B. Y., SIDDELL, S. G. & BRIERLEY, I. 2016. High-Resolution Analysis of Coronavirus Gene Expression by RNA Sequencing and Ribosome Profiling. *PLoS Pathog,* 12**,** e1005473.

JACKS, T., POWER, M. D., MASIARZ, F. R., LUCIW, P. A., BARR, P. J. & VARMUS, H. E. 1988. Characterization of ribosomal frameshifting in HIV-1 gag-pol expression. *Nature,* 331**,** 280-3.

JAFARZADEH, A., CHAUHAN, P., SAHA, B., JAFARZADEH, S. & NEMATI, M. 2020. Contribution of monocytes and macrophages to the local tissue inflammation and cytokine storm in COVID-19: Lessons from SARS and MERS, and potential therapeutic interventions. *Life Sci***,** 118102.

JAMES, C. C. & SMYTH, J. W. 2018. Alternative mechanisms of translation initiation: An emerging dynamic regulator of the proteome in health and disease. *Life Sci,* 212**,** 138-144.

KAMITANI, W., HUANG, C., NARAYANAN, K., LOKUGAMAGE, K. G. & MAKINO, S. 2009. A two-pronged strategy to suppress host protein synthesis by SARS coronavirus Nsp1 protein. *Nat Struct Mol Biol,* 16**,** 1134-40.

KIM, D., LEE, J. Y., YANG, J. S., KIM, J. W., KIM, V. N. & CHANG, H. 2020. The Architecture of SARS-CoV-2 Transcriptome. *Cell,* 181**,** 914-921 e10.

KOPECKY-BROMBERG, S. A., MARTINEZ-SOBRIDO, L. & PALESE, P. 2006. 7a protein of severe acute respiratory syndrome coronavirus inhibits cellular protein synthesis and activates p38 mitogen-activated protein kinase. *J Virol,* 80**,** 785-93.

KORNIY, N., SAMATOVA, E., ANOKHINA, M. M., PESKE, F. & RODNINA, M. V. 2019. Mechanisms and biomedical implications of -1 programmed ribosome frameshifting on viral and bacterial mRNAs. *FEBS Lett,* 593**,** 1468-1482.

KUTLUAY, S. B. & BIENIASZ, P. D. 2016. Analysis of HIV-1 Gag-RNA Interactions in Cells and Virions by CLIP-seq. *Methods Mol Biol,* 1354**,** 119-31.

KUTLUAY, S. B., ZANG, T., BLANCO-MELO, D., POWELL, C., JANNAIN, D., ERRANDO, M. & BIENIASZ, P. D. 2014. Global changes in the RNA binding specificity of HIV-1 gag regulate virion genesis. *Cell,* 159**,** 1096-1109.

KWAN, T. & THOMPSON, S. R. 2019. Noncanonical Translation Initiation in Eukaryotes. *Cold Spring Harb Perspect Biol,* 11.

LANGMEAD, B., TRAPNELL, C., POP, M. & SALZBERG, S. L. 2009. Ultrafast and memory-efficient alignment of short DNA sequences to the human genome. *Genome Biol,* 10**,** R25.

LAURIA, F., TEBALDI, T., BERNABO, P., GROEN, E. J. N., GILLINGWATER, T. H. & VIERO, G. 2018. riboWaltz: Optimization of ribosome P-site positioning in ribosome profiling data. *PLoS Comput Biol,* 14**,** e1006169.

LI, H. & DURBIN, R. 2009. Fast and accurate short read alignment with Burrows-Wheeler transform. *Bioinformatics,* 25**,** 1754-60.

LI, H., HANDSAKER, B., WYSOKER, A., FENNELL, T., RUAN, J., HOMER, N., MARTH, G., ABECASIS, G., DURBIN, R. & GENOME PROJECT DATA PROCESSING, S. 2009. The Sequence Alignment/Map format and SAMtools. *Bioinformatics,* 25**,** 2078-9.

LI, M. M., MACDONALD, M. R. & RICE, C. M. 2015. To translate, or not to translate: viral and host mRNA regulation by interferon-stimulated genes. *Trends Cell Biol,* 25**,** 320-9.

LI, Z., LI, Y., LIU, S. & QIN, Z. 2020. Extracellular S100A4 as a key player in fibrotic diseases. *J Cell Mol Med,* 24**,** 5973-5983.

LIU, Y., MYRVANG, H. K. & DEKKER, L. V. 2015. Annexin A2 complexes with S100 proteins: structure, function and pharmacological manipulation. *Br J Pharmacol,* 172**,** 1664-76.

LOKUGAMAGE, K. G., NARAYANAN, K., HUANG, C. & MAKINO, S. 2012. Severe acute respiratory syndrome coronavirus protein nsp1 is a novel eukaryotic translation inhibitor that represses multiple steps of translation initiation. *J Virol,* 86**,** 13598-608.

MASTERS, P. S. 2006. The molecular biology of coronaviruses. *Adv Virus Res,* 66**,** 193-292.

MENACHERY, V. D., EISFELD, A. J., SCHAFER, A., JOSSET, L., SIMS, A. C., PROLL, S., FAN, S., LI, C., NEUMANN, G., TILTON, S. C., CHANG, J., GRALINSKI, L. E., LONG, C., GREEN, R., WILLIAMS, C. M., WEISS, J., MATZKE, M. M., WEBB-ROBERTSON, B. J., SCHEPMOES, A. A., SHUKLA, A. K., METZ, T. O., SMITH, R. D., WATERS, K. M., KATZE, M. G., KAWAOKA, Y. & BARIC, R. S. 2014. Pathogenic influenza viruses and coronaviruses utilize similar and contrasting approaches to control interferon-stimulated gene responses. *mBio,* 5**,** e01174-14.

MITCHELL, H. D., EISFELD, A. J., SIMS, A. C., MCDERMOTT, J. E., MATZKE, M. M., WEBB-ROBERTSON, B. J., TILTON, S. C., TCHITCHEK, N., JOSSET, L., LI, C., ELLIS, A. L., CHANG, J. H., HEEGEL, R. A., LUNA, M. L., SCHEPMOES, A. A., SHUKLA, A. K., METZ, T. O., NEUMANN, G., BENECKE, A. G., SMITH, R. D., BARIC, R. S., KAWAOKA, Y., KATZE, M. G. & WATERS, K. M. 2013. A network integration approach to predict conserved regulators related to pathogenicity of influenza and SARS-CoV respiratory viruses. *PLoS One,* 8**,** e69374.

MOOTHA, V. K., LINDGREN, C. M., ERIKSSON, K. F., SUBRAMANIAN, A., SIHAG, S., LEHAR, J., PUIGSERVER, P., CARLSSON, E., RIDDERSTRALE, M., LAURILA, E., HOUSTIS, N., DALY, M. J., PATTERSON, N., MESIROV, J. P., GOLUB, T. R., TAMAYO, P., SPIEGELMAN, B., LANDER, E. S., HIRSCHHORN, J. N., ALTSHULER, D. & GROOP, L. C. 2003. PGC-1alpha-responsive genes involved in oxidative phosphorylation are coordinately downregulated in human diabetes. *Nat Genet,* 34**,** 267-73.

MOUZAKIS, K. D., LANG, A. L., VANDER MEULEN, K. A., EASTERDAY, P. D. & BUTCHER, S. E. 2013. HIV-1 frameshift efficiency is primarily determined by the stability of base pairs positioned at the mRNA entrance channel of the ribosome. *Nucleic Acids Res,* 41**,** 1901-13.

NAKAGAWA, K., LOKUGAMAGE, K. G. & MAKINO, S. 2016. Viral and Cellular mRNA Translation in Coronavirus-Infected Cells. *Adv Virus Res,* 96**,** 165-192.

NARAYANAN, K., HUANG, C., LOKUGAMAGE, K., KAMITANI, W., IKEGAMI, T., TSENG, C. T. & MAKINO, S. 2008. Severe acute respiratory syndrome coronavirus nsp1 suppresses host gene expression, including that of type I interferon, in infected cells. *J Virol,* 82**,** 4471-9.

NARAYANAN, K., RAMIREZ, S. I., LOKUGAMAGE, K. G. & MAKINO, S. 2015. Coronavirus nonstructural protein 1: Common and distinct functions in the regulation of host and viral gene expression. *Virus Res,* 202**,** 89-100.

PARKIN, N. T., CHAMORRO, M. & VARMUS, H. E. 1992. Human immunodeficiency virus type 1 gag-pol frameshifting is dependent on downstream mRNA secondary structure: demonstration by expression in vivo. *J Virol,* 66**,** 5147-51.

PERLMAN, S. & DANDEKAR, A. A. 2005. Immunopathogenesis of coronavirus infections: implications for SARS. *Nat Rev Immunol,* 5**,** 917-27.

PLANT, E. P. & DINMAN, J. D. 2008. The role of programmed-1 ribosomal frameshifting in coronavirus propagation. *Front Biosci,* 13**,** 4873-81.

PLANT, E. P., JACOBS, K. L., HARGER, J. W., MESKAUSKAS, A., JACOBS, J. L., BAXTER, J. L., PETROV, A. N. & DINMAN, J. D. 2003. The 9-A solution: how mRNA pseudoknots promote efficient programmed -1 ribosomal frameshifting. *RNA,* 9**,** 168-74.

RAO, S., HOSKINS, I., GARCIA, P. D., TONN, T., OZADAM, H., CENIK, E. S. & CENIK, C. 2020. Genes with 5' terminal oligopyrimidine tracts preferentially escape global suppression of translation by the SARS-CoV-2 NSP1 protein. *bioRxiv*.

REYNAUD, J. M., KIM, D. Y., ATASHEVA, S., RASALOUSKAYA, A., WHITE, J. P., DIAMOND, M. S., WEAVER, S. C., FROLOVA, E. I. & FROLOV, I. 2015. IFIT1 Differentially Interferes with Translation and Replication of Alphavirus Genomes and Promotes Induction of Type I Interferon. *PLoS Pathog,* 11**,** e1004863.

RIBA, A., DI NANNI, N., MITTAL, N., ARHNE, E., SCHMIDT, A. & ZAVOLAN, M. 2019. Protein synthesis rates and ribosome occupancies reveal determinants of translation elongation rates. *Proc Natl Acad Sci U S A,* 116**,** 15023-15032.

ROBINSON, M. D., MCCARTHY, D. J. & SMYTH, G. K. 2010. edgeR: a Bioconductor package for differential expression analysis of digital gene expression data. *Bioinformatics,* 26**,** 139-40.

SCHUBERT, K., KAROUSIS, E. D., JOMAA, A., SCAIOLA, A., ECHEVERRIA, B., GURZELER, L. A., LEIBUNDGUT, M., THIEL, V., MUHLEMANN, O. & BAN, N. 2020. SARS-CoV-2 Nsp1 binds the ribosomal mRNA channel to inhibit translation. *Nat Struct Mol Biol,* 27**,** 959-966.

SHEHU-XHILAGA, M., CROWE, S. M. & MAK, J. 2001. Maintenance of the Gag/Gag-Pol ratio is important for human immunodeficiency virus type 1 RNA dimerization and viral infectivity. *J Virol,* 75**,** 1834-41.

STAPLE, D. W. & BUTCHER, S. E. 2005. Solution structure and thermodynamic investigation of the HIV-1 frameshift inducing element. *J Mol Biol,* 349**,** 1011-23.

SUBRAMANIAN, A., TAMAYO, P., MOOTHA, V. K., MUKHERJEE, S., EBERT, B. L., GILLETTE, M. A., PAULOVICH, A., POMEROY, S. L., GOLUB, T. R., LANDER, E. S.

& MESIROV, J. P. 2005. Gene set enrichment analysis: a knowledge-based approach for interpreting genome-wide expression profiles. *Proc Natl Acad Sci U S A,* 102**,** 15545-50.

TAYLOR, J. R., SKEATE, J. G. & KAST, W. M. 2018. Annexin A2 in Virus Infection. *Front Microbiol,* 9**,** 2954.

TENENBAUM, D. 2020. KEGGREST: Client-side REST access to KEGG. R package version 1.6.4.

WANG, X., XUAN, Y., HAN, Y., DING, X., YE, K., YANG, F., GAO, P., GOFF, S. P. & GAO, G. 2019. Regulation of HIV-1 Gag-Pol Expression by Shiftless, an Inhibitor of Programmed -1 Ribosomal Frameshifting. *Cell,* 176**,** 625-635 e14.

WEISS, S. R. & NAVAS-MARTIN, S. 2005. Coronavirus pathogenesis and the emerging pathogen severe acute respiratory syndrome coronavirus. *Microbiol Mol Biol Rev,* 69**,** 635-64.

WILK, A. J., RUSTAGI, A., ZHAO, N. Q., ROQUE, J., MARTINEZ-COLON, G. J., MCKECHNIE, J. L., IVISON, G. T., RANGANATH, T., VERGARA, R., HOLLIS, T., SIMPSON, L. J., GRANT, P., SUBRAMANIAN, A., ROGERS, A. J. & BLISH, C. A. 2020. A single-cell atlas of the peripheral immune response in patients with severe COVID-19. *Nat Med,* 26**,** 1070-1076.

WILSON, W., BRADDOCK, M., ADAMS, S. E., RATHJEN, P. D., KINGSMAN, S. M. & KINGSMAN, A. J. 1988. HIV expression strategies: ribosomal frameshifting is directed by a short sequence in both mammalian and yeast systems. *Cell,* 55**,** 1159-69.

XIAO, H., XU, L. H., YAMADA, Y. & LIU, D. X. 2008. Coronavirus spike protein inhibits host cell translation by interaction with eIF3f. *PLoS One,* 3**,** e1494.

XIE, X., MURUATO, A., LOKUGAMAGE, K. G., NARAYANAN, K., ZHANG, X., ZOU, J., LIU, J., SCHINDEWOLF, C., BOPP, N. E., AGUILAR, P. V., PLANTE, K. S., WEAVER, S. C., MAKINO, S., LEDUC, J. W., MENACHERY, V. D. & SHI, P. Y. 2020. An Infectious cDNA Clone of SARS-CoV-2. *Cell Host Microbe,* 27**,** 841-848 e3.

YOU, Y., RICHER, E. J., HUANG, T. & BRODY, S. L. 2002. Growth and differentiation of mouse tracheal epithelial cells: selection of a proliferative population. *Am J Physiol Lung Cell Mol Physiol,* 283**,** L1315-21.

YOUNG, M. D., WAKEFIELD, M. J., SMYTH, G. K. & OSHLACK, A. 2010. Gene ontology analysis for RNA-seq: accounting for selection bias. *Genome Biol,* 11**,** R14.

ZHANG, P., HE, D., XU, Y., HOU, J., PAN, B. F., WANG, Y., LIU, T., DAVIS, C. M., EHLI, E. A., TAN, L., ZHOU, F., HU, J., YU, Y., CHEN, X., NGUYEN, T. M., ROSEN, J. M., HAWKE, D. H., JI, Z. & CHEN, Y. 2017. Genome-wide identification and differential analysis of translational initiation. *Nat Commun,* 8**,** 1749.

ZHOU, B., LIU, J., WANG, Q., LIU, X., LI, X., LI, P., MA, Q. & CAO, C. 2008. The nucleocapsid protein of severe acute respiratory syndrome coronavirus inhibits cell cytokinesis and proliferation by interacting with translation elongation factor 1alpha. *J Virol,* 82**,** 6962-71.

ZHOU, Z., REN, L., ZHANG, L., ZHONG, J., XIAO, Y., JIA, Z., GUO, L., YANG, J., WANG, C., JIANG, S., YANG, D., ZHANG, G., LI, H., CHEN, F., XU, Y., CHEN, M., GAO, Z., YANG, J., DONG, J., LIU, B., ZHANG, X., WANG, W., HE, K., JIN, Q., LI, M. & WANG, J. 2020. Heightened Innate Immune Responses in the Respiratory Tract of COVID-19 Patients. *Cell Host Microbe,* 27**,** 883-890 e2.

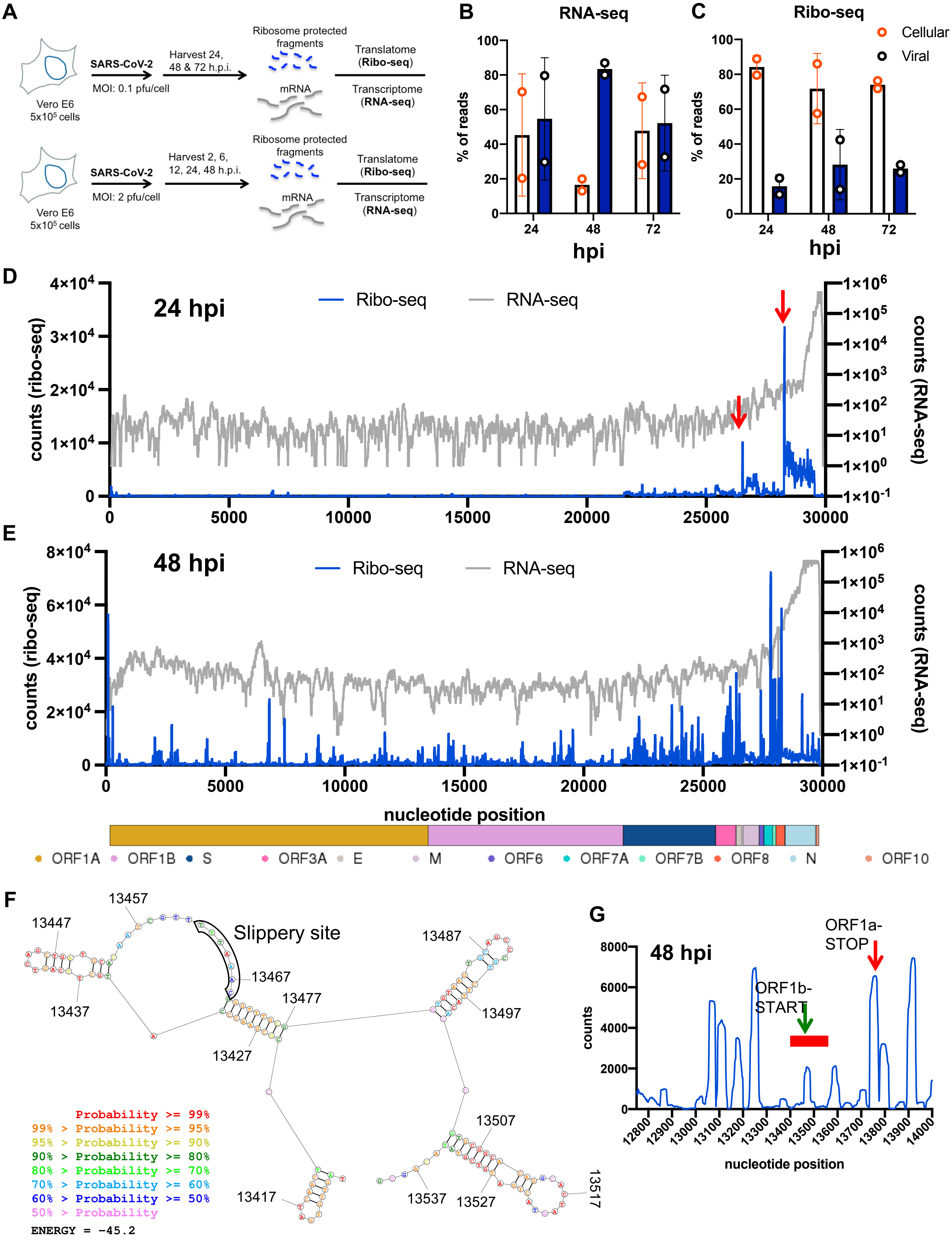
A
Vero E6
5x10⁵ cells
SARS-CoV-2
MOI: 0.1 pfu/cell
Harvest 24, 48 & 72 h.p.i.
Ribosome protected fragments
mRNA
Translatome (Ribo-seq)
Transcriptome (RNA-seq)
Vero E6
5x10⁵ cells
SARS-CoV-2
MOI: 2 pfu/cell
Harvest 2, 6, 12, 24, 48 h.p.i.
Ribosome protected fragments
mRNA
Translatome (Ribo-seq)
Transcriptome (RNA-seq)
B
RNA-seq
% of reads
0
20
40
60
80
100
24
48
72
hpi
C
Ribo-seq
Cellular
Viral
% of reads
0
20
40
60
80
100
24
48
72
hpi
D
24 hpi
Ribo-seq
RNA-seq
counts (ribo-seq)
0
1×10⁴
2×10⁴
3×10⁴
4×10⁴
counts (RNA-seq)
1×10⁻¹
1×10⁰
1×10¹
1×10²
1×10³
1×10⁴
1×10⁵
1×10⁶
0
5000
10000
15000
20000
25000
30000
E
48 hpi
Ribo-seq
RNA-seq
counts (ribo-seq)
0
2×10⁴
4×10⁴
6×10⁴
8×10⁴
counts (RNA-seq)
1×10⁻¹
1×10⁰
1×10¹
1×10²
1×10³
1×10⁴
1×10⁵
1×10⁶
0
5000
10000
15000
20000
25000
30000
nucleotide position
ORF1A
ORF1B
S
ORF3A
E
M
ORF6
ORF7A
ORF7B
ORF8
N
ORF10
F
13447
13457
Slippery site
13467
13437
13477
13427
13487
13497
13417
13507
13537
13527
13517
Probability >= 99%
99% > Probability >= 95%
95% > Probability >= 90%
90% > Probability >= 80%
80% > Probability >= 70%
70% > Probability >= 60%
60% > Probability >= 50%
50% > Probability
ENERGY = -45.2
G
48 hpi
ORF1a-STOP
ORF1b-START
counts
0
2000
4000
6000
8000
12800
12900
13000
13100
13200
13300
13400
13500
13600
13700
13800
13900
14000
nucleotide position

Figure 1

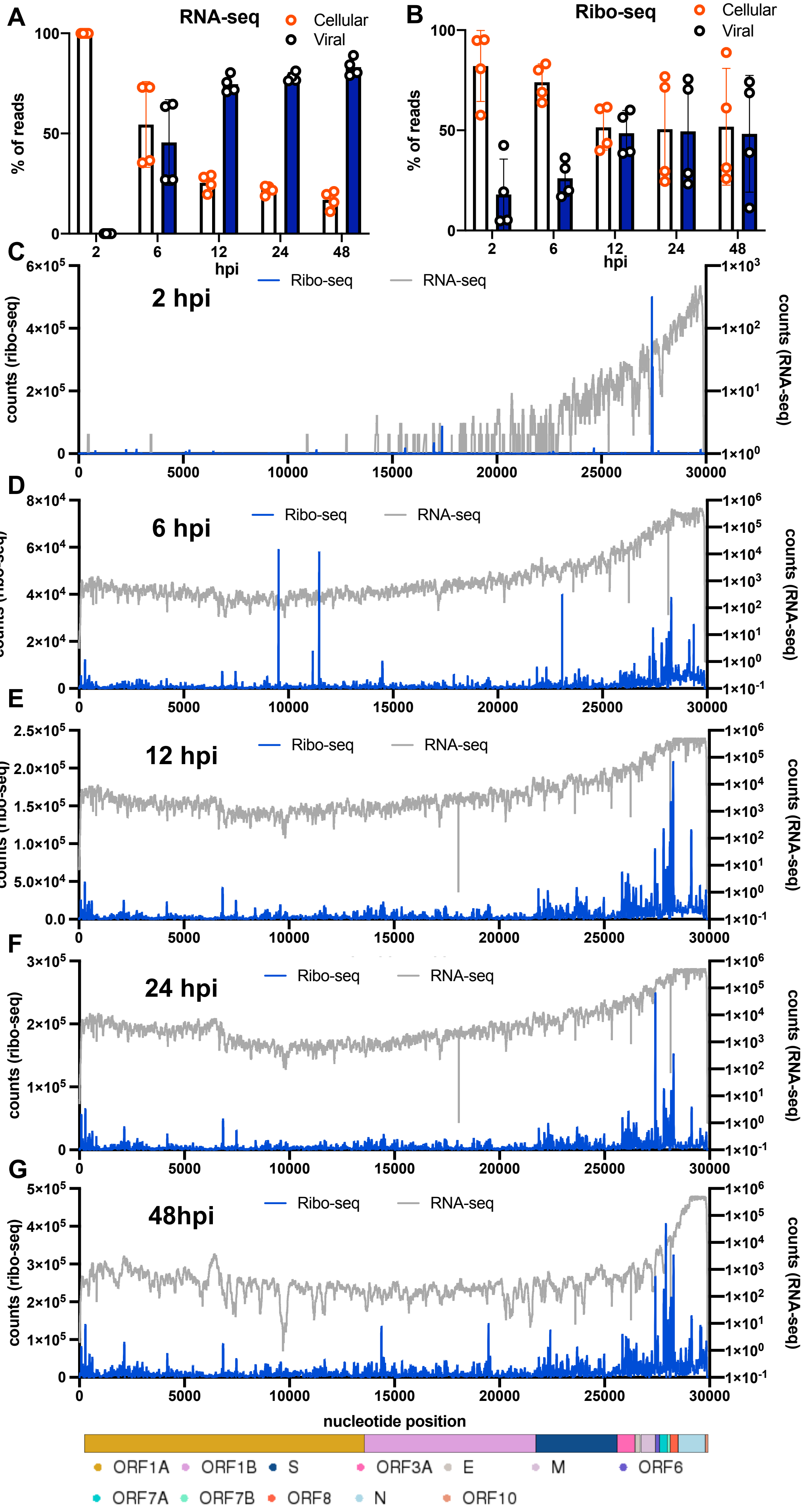
A
RNA-seq
Cellular
Viral
% of reads
100
50
0
2
6
12
24
48
hpi
B
Ribo-seq
Cellular
Viral
% of reads
100
50
0
2
6
12
24
48
hpi
C
2 hpi
Ribo-seq
RNA-seq
counts (ribo-seq)
counts (RNA-seq)
6×10^5
4×10^5
2×10^5
0
1×10^3
1×10^2
1×10^1
1×10^0
0
5000
10000
15000
20000
25000
30000
D
6 hpi
Ribo-seq
RNA-seq
counts (ribo-seq)
counts (RNA-seq)
8×10^4
6×10^4
4×10^4
2×10^4
0
1×10^6
1×10^5
1×10^4
1×10^3
1×10^2
1×10^1
1×10^0
1×10^{-1}
0
5000
10000
15000
20000
25000
30000
E
12 hpi
Ribo-seq
RNA-seq
counts (ribo-seq)
counts (RNA-seq)
2.5×10^5
2.0×10^5
1.5×10^5
1.0×10^5
5.0×10^4
0.0
1×10^6
1×10^5
1×10^4
1×10^3
1×10^2
1×10^1
1×10^0
1×10^{-1}
0
5000
10000
15000
20000
25000
30000
F
24 hpi
Ribo-seq
RNA-seq
counts (ribo-seq)
counts (RNA-seq)
3×10^5
2×10^5
1×10^5
0
1×10^6
1×10^5
1×10^4
1×10^3
1×10^2
1×10^1
1×10^0
1×10^{-1}
0
5000
10000
15000
20000
25000
30000
G
48hpi
Ribo-seq
RNA-seq
counts (ribo-seq)
counts (RNA-seq)
5×10^5
4×10^5
3×10^5
2×10^5
1×10^5
0
1×10^6
1×10^5
1×10^4
1×10^3
1×10^2
1×10^1
1×10^0
1×10^{-1}
0
5000
10000
15000
20000
25000
30000
nucleotide position
ORF1A
ORF1B
S
ORF3A
E
M
ORF6
ORF7A
ORF7B
ORF8
N
ORF10

Figure 2

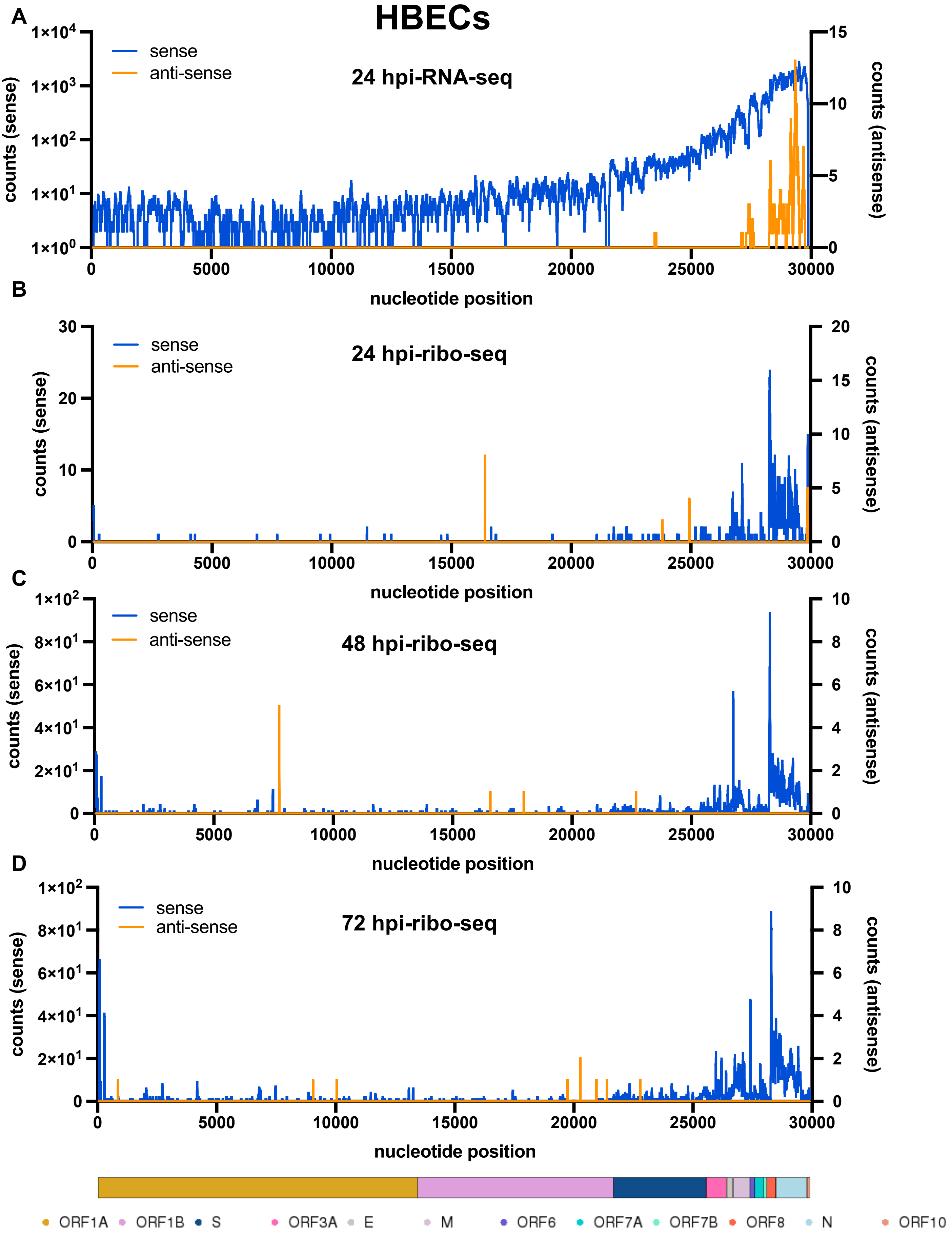
HBECs
A
24 hpi-RNA-seq
sense
anti-sense
counts (sense)
counts (antisense)
1×10^4
1×10^3
1×10^2
1×10^1
1×10^0
15
10
5
0
0
5000
10000
15000
20000
25000
30000
nucleotide position
B
24 hpi-ribo-seq
sense
anti-sense
counts (sense)
counts (antisense)
30
20
10
0
20
15
10
5
0
nucleotide position
C
48 hpi-ribo-seq
sense
anti-sense
counts (sense)
counts (antisense)
1×10^2
8×10^1
6×10^1
4×10^1
2×10^1
0
10
8
6
4
2
0
nucleotide position
D
72 hpi-ribo-seq
sense
anti-sense
counts (sense)
counts (antisense)
1×10^2
8×10^1
6×10^1
4×10^1
2×10^1
0
10
8
6
4
2
0
nucleotide position
ORF1A
ORF1B
S
ORF3A
E
M
ORF6
ORF7A
ORF7B
ORF8
N
ORF10

Figure 3

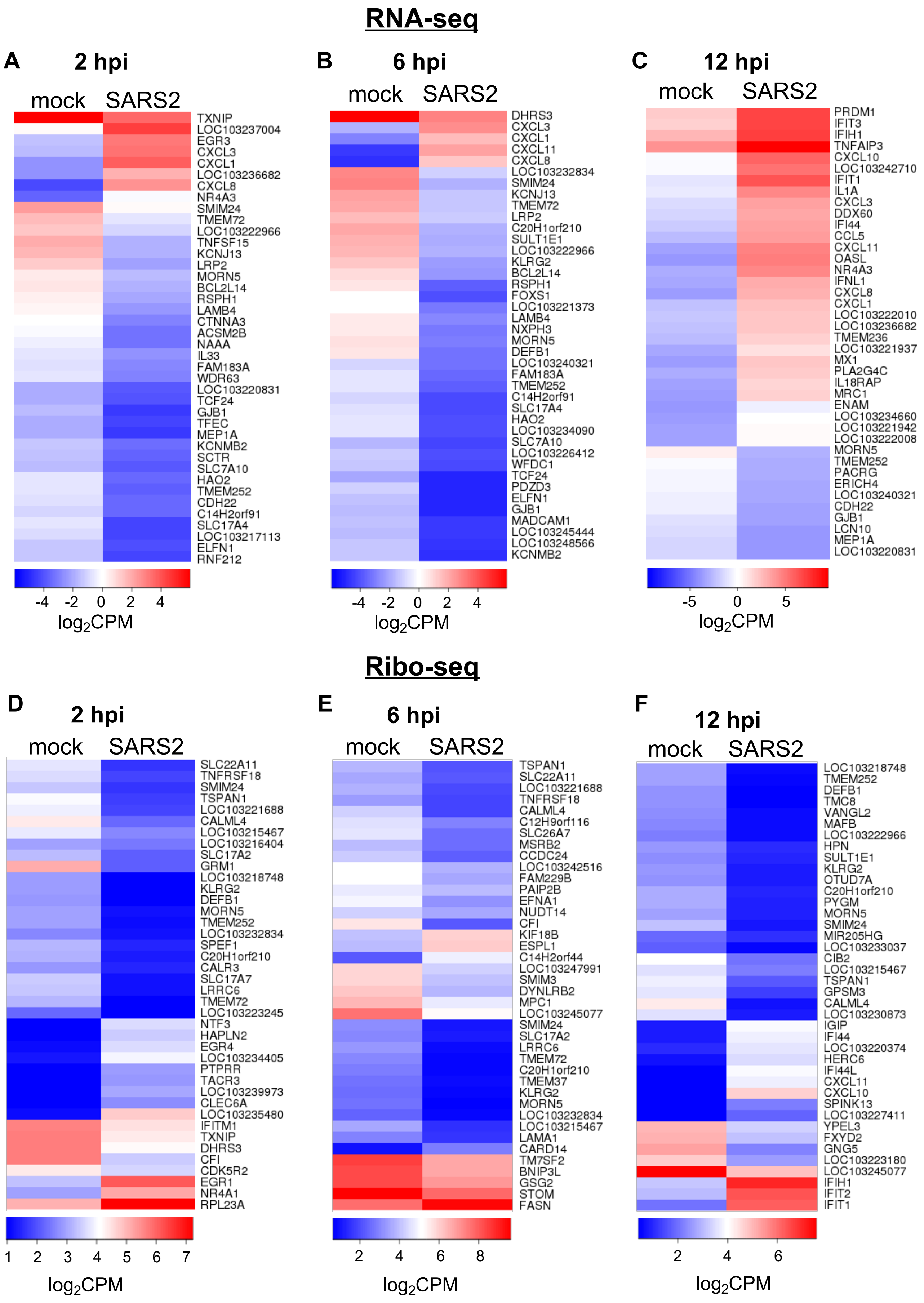
RNA-seq
A
2 hpi
mock
SARS2
TXNIP
LOC103237004
EGR3
CXCL3
CXCL1
LOC103236682
CXCL8
NR4A3
SMIM24
TMEM72
LOC103222966
TNFSF15
KCNJ13
LRP2
MORN5
BCL2L14
RSPH1
LAMB4
CTNNA3
ACSM2B
NAAA
IL33
FAM183A
WDR63
LOC103220831
TCF24
GJB1
TFEC
MEP1A
KCNMB2
SCTR
SLC7A10
HAO2
TMEM252
CDH22
C14H2orf91
SLC17A4
LOC103217113
ELFN1
RNF212
-4
-2
0
2
4
log$_2$CPM
B
6 hpi
mock
SARS2
DHRS3
CXCL3
CXCL1
CXCL11
CXCL8
LOC103232834
SMIM24
KCNJ13
TMEM72
LRP2
C20H1orf210
SULT1E1
LOC103222966
KLRG2
BCL2L14
RSPH1
FOXS1
LOC103221373
LAMB4
NXPH3
MORN5
DEFB1
LOC103240321
FAM183A
TMEM252
C14H2orf91
SLC17A4
HAO2
LOC103234090
SLC7A10
LOC103226412
WFDC1
TCF24
PDZD3
ELFN1
GJB1
MADCAM1
LOC103245444
LOC103248566
KCNMB2
-4
-2
0
2
4
log$_2$CPM
C
12 hpi
mock
SARS2
PRDM1
IFIT3
IFIH1
TNFAIP3
CXCL10
LOC103242710
IFIT1
IL1A
CXCL3
DDX60
IFI44
CCL5
CXCL11
OASL
NR4A3
IFNL1
CXCL8
CXCL1
LOC103222010
LOC103236682
TMEM236
LOC103221937
MX1
PLA2G4C
IL18RAP
MRC1
ENAM
LOC103234660
LOC103221942
LOC103222008
MORN5
TMEM252
PACRG
ERICH4
LOC103240321
CDH22
GJB1
LCN10
MEP1A
LOC103220831
-5
0
5
log$_2$CPM
Ribo-seq
D
2 hpi
mock
SARS2
SLC22A11
TNFRSF18
SMIM24
TSPAN1
LOC103221688
CALML4
LOC103215467
LOC103216404
SLC17A2
GRM1
LOC103218748
KLRG2
DEFB1
MORN5
TMEM252
LOC103232834
SPEF1
C20H1orf210
CALR3
SLC17A7
LRRC6
TMEM72
LOC103223245
NTF3
HAPLN2
EGR4
LOC103234405
PTPRR
TACR3
LOC103239973
CLEC6A
LOC103235480
IFITM1
TXNIP
DHRS3
CFI
CDK5R2
EGR1
NR4A1
RPL23A
1
2
3
4
5
6
7
log$_2$CPM
E
6 hpi
mock
SARS2
TSPAN1
SLC22A11
LOC103221688
TNFRSF18
CALML4
C12H9orf116
SLC26A7
MSRB2
CCDC24
LOC103242516
FAM229B
PAIP2B
EFNA1
NUDT14
CFI
KIF18B
ESPL1
C14H2orf44
LOC103247991
SMIM3
DYNLRB2
MPC1
LOC103245077
SMIM24
SLC17A2
LRRC6
TMEM72
C20H1orf210
TMEM37
KLRG2
MORN5
LOC103232834
LOC103215467
LAMA1
CARD14
TM7SF2
BNIP3L
GSG2
STOM
FASN
2
4
6
8
log$_2$CPM
F
12 hpi
mock
SARS2
LOC103218748
TMEM252
DEFB1
TMC8
VANGL2
MAFB
LOC103222966
HPN
SULT1E1
KLRG2
OTUD7A
C20H1orf210
PYGM
MORN5
SMIM24
MIR205HG
LOC103233037
CIB2
LOC103215467
TSPAN1
GPSM3
CALML4
LOC103230873
IGIP
IFI44
LOC103220374
HERC6
IFI44L
CXCL11
CXCL10
SPINK13
LOC103227411
YPEL3
FXYD2
GNG5
LOC103223180
LOC103245077
IFIH1
IFIT2
IFIT1
2
4
6
log$_2$CPM

Figure 4

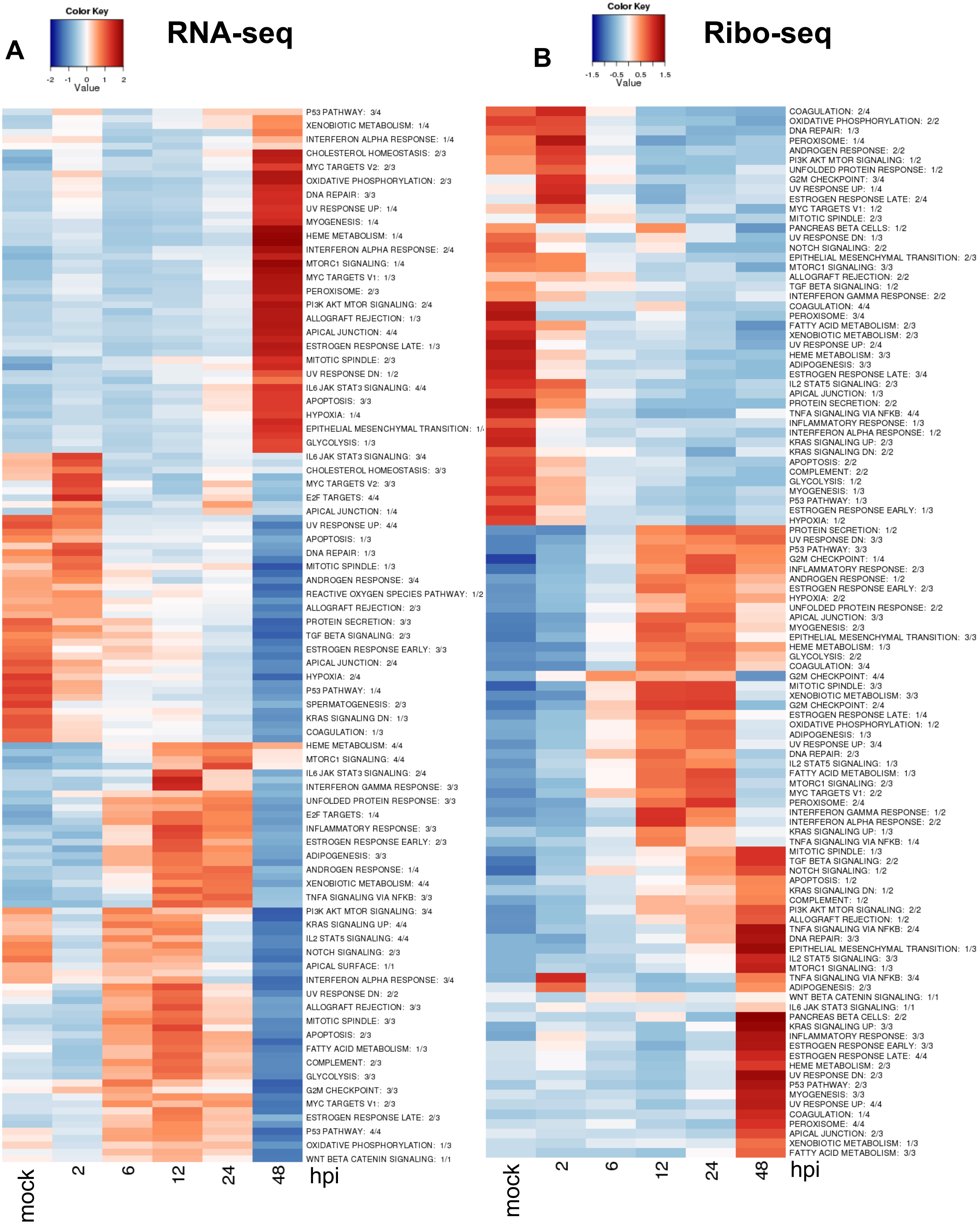
A
Color Key
-2
-1
0
1
2
Value
RNA-seq
P53 PATHWAY: 3/4
XENOBIOTIC METABOLISM: 1/4
INTERFERON ALPHA RESPONSE: 1/4
CHOLESTEROL HOMEOSTASIS: 2/3
MYC TARGETS V2: 2/3
OXIDATIVE PHOSPHORYLATION: 2/3
DNA REPAIR: 3/3
UV RESPONSE UP: 1/4
MYOGENESIS: 1/4
HEME METABOLISM: 1/4
INTERFERON ALPHA RESPONSE: 2/4
MTORC1 SIGNALING: 1/4
MYC TARGETS V1: 1/3
PEROXISOME: 2/3
PI3K AKT MTOR SIGNALING: 2/4
ALLOGRAFT REJECTION: 1/3
APICAL JUNCTION: 4/4
ESTROGEN RESPONSE LATE: 1/3
MITOTIC SPINDLE: 2/3
UV RESPONSE DN: 1/2
IL6 JAK STAT3 SIGNALING: 4/4
APOPTOSIS: 3/3
HYPOXIA: 1/4
EPITHELIAL MESENCHYMAL TRANSITION: 1/
GLYCOLYSIS: 1/3
IL6 JAK STAT3 SIGNALING: 3/4
CHOLESTEROL HOMEOSTASIS: 3/3
MYC TARGETS V2: 3/3
E2F TARGETS: 4/4
APICAL JUNCTION: 1/4
UV RESPONSE UP: 4/4
APOPTOSIS: 1/3
DNA REPAIR: 1/3
MITOTIC SPINDLE: 1/3
ANDROGEN RESPONSE: 3/4
REACTIVE OXYGEN SPECIES PATHWAY: 1/2
ALLOGRAFT REJECTION: 2/3
PROTEIN SECRETION: 3/3
TGF BETA SIGNALING: 2/3
ESTROGEN RESPONSE EARLY: 3/3
APICAL JUNCTION: 2/4
HYPOXIA: 2/4
P53 PATHWAY: 1/4
SPERMATOGENESIS: 2/3
KRAS SIGNALING DN: 1/3
COAGULATION: 1/3
HEME METABOLISM: 4/4
MTORC1 SIGNALING: 4/4
IL6 JAK STAT3 SIGNALING: 2/4
INTERFERON GAMMA RESPONSE: 3/3
UNFOLDED PROTEIN RESPONSE: 3/3
E2F TARGETS: 1/4
INFLAMMATORY RESPONSE: 3/3
ESTROGEN RESPONSE EARLY: 2/3
ADIPOGENESIS: 3/3
ANDROGEN RESPONSE: 1/4
XENOBIOTIC METABOLISM: 4/4
TNFA SIGNALING VIA NFKB: 3/3
PI3K AKT MTOR SIGNALING: 3/4
KRAS SIGNALING UP: 4/4
IL2 STAT5 SIGNALING: 4/4
NOTCH SIGNALING: 2/3
APICAL SURFACE: 1/1
INTERFERON ALPHA RESPONSE: 3/4
UV RESPONSE DN: 2/2
ALLOGRAFT REJECTION: 3/3
MITOTIC SPINDLE: 3/3
APOPTOSIS: 2/3
FATTY ACID METABOLISM: 1/3
COMPLEMENT: 2/3
GLYCOLYSIS: 3/3
G2M CHECKPOINT: 3/3
MYC TARGETS V1: 2/3
ESTROGEN RESPONSE LATE: 2/3
P53 PATHWAY: 4/4
OXIDATIVE PHOSPHORYLATION: 1/3
WNT BETA CATENIN SIGNALING: 1/1
mock
2
6
12
24
48
hpi
B
Color Key
-1.5
-0.5
0.5
1.5
Value
Ribo-seq
COAGULATION: 2/4
OXIDATIVE PHOSPHORYLATION: 2/2
DNA REPAIR: 1/3
PEROXISOME: 1/4
ANDROGEN RESPONSE: 2/2
PI3K AKT MTOR SIGNALING: 1/2
UNFOLDED PROTEIN RESPONSE: 1/2
G2M CHECKPOINT: 3/4
UV RESPONSE UP: 1/4
ESTROGEN RESPONSE LATE: 2/4
MYC TARGETS V1: 1/2
MITOTIC SPINDLE: 2/3
PANCREAS BETA CELLS: 1/2
UV RESPONSE DN: 1/3
NOTCH SIGNALING: 2/2
EPITHELIAL MESENCHYMAL TRANSITION: 2/3
MTORC1 SIGNALING: 3/3
ALLOGRAFT REJECTION: 2/2
TGF BETA SIGNALING: 1/2
INTERFERON GAMMA RESPONSE: 2/2
COAGULATION: 4/4
PEROXISOME: 3/4
FATTY ACID METABOLISM: 2/3
XENOBIOTIC METABOLISM: 2/3
UV RESPONSE UP: 2/4
HEME METABOLISM: 3/3
ADIPOGENESIS: 3/3
ESTROGEN RESPONSE LATE: 3/4
IL2 STAT5 SIGNALING: 2/3
APICAL JUNCTION: 1/3
PROTEIN SECRETION: 2/2
TNFA SIGNALING VIA NFKB: 4/4
INFLAMMATORY RESPONSE: 1/3
INTERFERON ALPHA RESPONSE: 1/2
KRAS SIGNALING UP: 2/3
KRAS SIGNALING DN: 2/2
APOPTOSIS: 2/2
COMPLEMENT: 2/2
GLYCOLYSIS: 1/2
MYOGENESIS: 1/3
P53 PATHWAY: 1/3
ESTROGEN RESPONSE EARLY: 1/3
HYPOXIA: 1/2
PROTEIN SECRETION: 1/2
UV RESPONSE DN: 3/3
P53 PATHWAY: 3/3
G2M CHECKPOINT: 1/4
INFLAMMATORY RESPONSE: 2/3
ANDROGEN RESPONSE: 1/2
ESTROGEN RESPONSE EARLY: 2/3
HYPOXIA: 2/2
UNFOLDED PROTEIN RESPONSE: 2/2
APICAL JUNCTION: 3/3
MYOGENESIS: 2/3
EPITHELIAL MESENCHYMAL TRANSITION: 3/3
HEME METABOLISM: 1/3
GLYCOLYSIS: 2/2
COAGULATION: 3/4
G2M CHECKPOINT: 4/4
MITOTIC SPINDLE: 3/3
XENOBIOTIC METABOLISM: 3/3
G2M CHECKPOINT: 2/4
ESTROGEN RESPONSE LATE: 1/4
OXIDATIVE PHOSPHORYLATION: 1/2
ADIPOGENESIS: 1/3
UV RESPONSE UP: 3/4
DNA REPAIR: 2/3
IL2 STAT5 SIGNALING: 1/3
FATTY ACID METABOLISM: 1/3
MTORC1 SIGNALING: 2/3
MYC TARGETS V1: 2/2
PEROXISOME: 2/4
INTERFERON GAMMA RESPONSE: 1/2
INTERFERON ALPHA RESPONSE: 2/2
KRAS SIGNALING UP: 1/3
TNFA SIGNALING VIA NFKB: 1/4
MITOTIC SPINDLE: 1/3
TGF BETA SIGNALING: 2/2
NOTCH SIGNALING: 1/2
APOPTOSIS: 1/2
KRAS SIGNALING DN: 1/2
COMPLEMENT: 1/2
PI3K AKT MTOR SIGNALING: 2/2
ALLOGRAFT REJECTION: 1/2
TNFA SIGNALING VIA NFKB: 2/4
DNA REPAIR: 3/3
EPITHELIAL MESENCHYMAL TRANSITION: 1/3
IL2 STAT5 SIGNALING: 3/3
MTORC1 SIGNALING: 1/3
TNFA SIGNALING VIA NFKB: 3/4
ADIPOGENESIS: 2/3
WNT BETA CATENIN SIGNALING: 1/1
IL6 JAK STAT3 SIGNALING: 1/1
PANCREAS BETA CELLS: 2/2
KRAS SIGNALING UP: 3/3
INFLAMMATORY RESPONSE: 3/3
ESTROGEN RESPONSE EARLY: 3/3
ESTROGEN RESPONSE LATE: 4/4
HEME METABOLISM: 2/3
UV RESPONSE DN: 2/3
P53 PATHWAY: 2/3
MYOGENESIS: 3/3
UV RESPONSE UP: 4/4
COAGULATION: 1/4
PEROXISOME: 4/4
APICAL JUNCTION: 2/3
XENOBIOTIC METABOLISM: 1/3
FATTY ACID METABOLISM: 3/3
mock
2
6
12
24
48
hpi

Figure 5

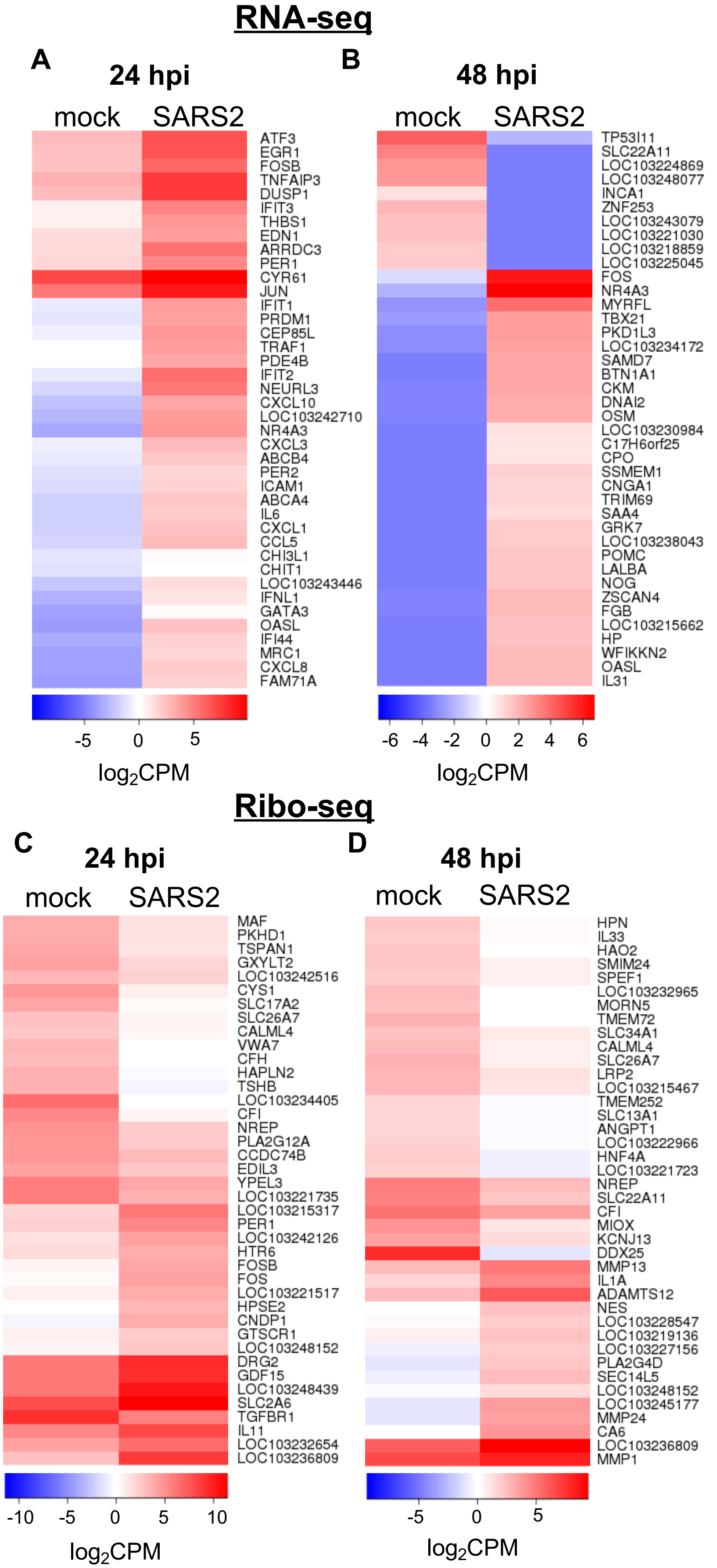
RNA-seq
A
24 hpi
mock
SARS2
ATF3
EGR1
FOSB
TNFAIP3
DUSP1
IFIT3
THBS1
EDN1
ARRDC3
PER1
CYR61
JUN
IFIT1
PRDM1
CEP85L
TRAF1
PDE4B
IFIT2
NEURL3
CXCL10
LOC103242710
NR4A3
CXCL3
ABCB4
PER2
ICAM1
ABCA4
IL6
CXCL1
CCL5
CHI3L1
CHIT1
LOC103243446
IFNL1
GATA3
OASL
IFI44
MRC1
CXCL8
FAM71A
-5
0
5
log$_2$CPM
B
48 hpi
mock
SARS2
TP53I11
SLC22A11
LOC103224869
LOC103248077
INCA1
ZNF253
LOC103243079
LOC103221030
LOC103218859
LOC103225045
FOS
NR4A3
MYRFL
TBX21
PKD1L3
LOC103234172
SAMD7
BTN1A1
CKM
DNAI2
OSM
LOC103230984
C17H6orf25
CPO
SSMEM1
CNGA1
TRIM69
SAA4
GRK7
LOC103238043
POMC
LALBA
NOG
ZSCAN4
FGB
LOC103215662
HP
WFIKKN2
OASL
IL31
-6
-4
-2
0
2
4
6
log$_2$CPM
Ribo-seq
C
24 hpi
mock
SARS2
MAF
PKHD1
TSPAN1
GXYLT2
LOC103242516
CYS1
SLC17A2
SLC26A7
CALML4
VWA7
CFH
HAPLN2
TSHB
LOC103234405
CFI
NREP
PLA2G12A
CCDC74B
EDIL3
YPEL3
LOC103221735
LOC103215317
PER1
LOC103242126
HTR6
FOSB
FOS
LOC103221517
HPSE2
CNDP1
GTSCR1
LOC103248152
DRG2
GDF15
LOC103248439
SLC2A6
TGFBR1
IL11
LOC103232654
LOC103236809
-10
-5
0
5
10
log$_2$CPM
D
48 hpi
mock
SARS2
HPN
IL33
HAO2
SMIM24
SPEF1
LOC103232965
MORN5
TMEM72
SLC34A1
CALML4
SLC26A7
LRP2
LOC103215467
TMEM252
SLC13A1
ANGPT1
LOC103222966
HNF4A
LOC103221723
NREP
SLC22A11
CFI
MIOX
KCNJ13
DDX25
MMP13
IL1A
ADAMTS12
NES
LOC103228547
LOC103219136
LOC103227156
PLA2G4D
SEC14L5
LOC103248152
LOC103245177
MMP24
CA6
LOC103236809
MMP1
-5
0
5
log$_2$CPM

Figure 6

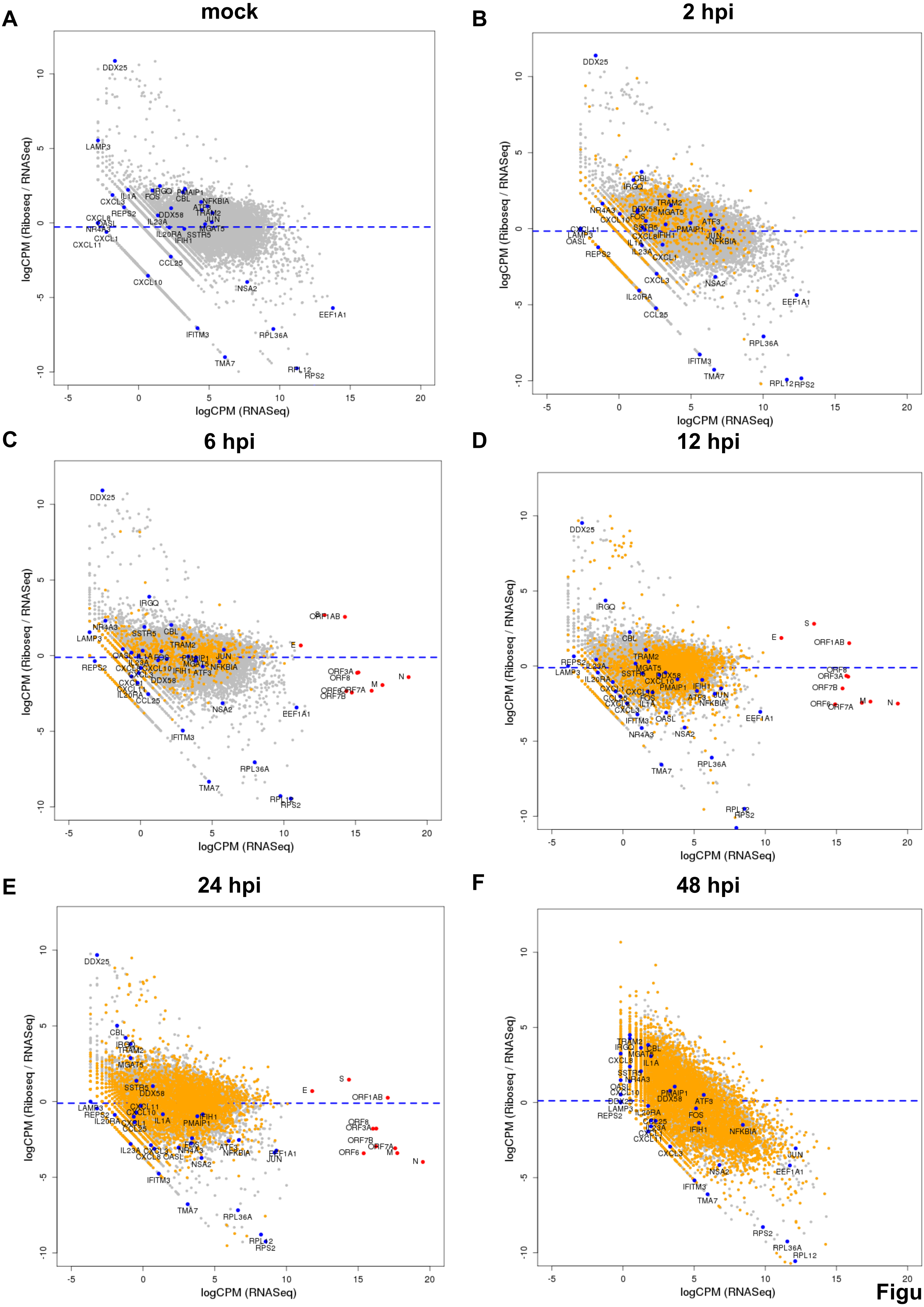
A
mock
B
2 hpi
C
6 hpi
D
12 hpi
E
24 hpi
F
48 hpi
logCPM (Riboseq / RNASeq)
logCPM (RNASeq)
-5
0
5
10
15
20
-10
DDX25
LAMP3
IRGQ
FOS
PMAIP1
CBL
NFKBIA
ATF3
TRAM2
JUN
MGAT5
SSTR5
IFIH1
IL20RA
IL23A
DDX58
IL1A
CXCL3
REPS2
CXCL8
OASL
NR4A3
CXCL1
CXCL11
CCL25
CXCL10
NSA2
EEF1A1
IFITM3
RPL36A
TMA7
RPL12
RPS2
S
E
ORF1AB
ORF3A
ORF8
ORF6
ORF7A
ORF7B
M
N

Figure 7